DOI: 10.1002/((please add manuscript number))
Article type: Communication

Enhancing fullerene-based solar cell lifetimes by addition of a fullerene dumbbell

Bob C. Schroeder, Zhe Li,* Michael A. Brady, Gregório Faria, Raja Shahid Ashraf, Christopher J. Takacs, Duc T. Duong, Kar Ho Chiu, Ching-Hong Tan, João T. Cabral, Alberto Salleo, Michael L. Chabinyc, James R. Durrant, and Iain McCulloch*

Dr. B. C. Schroeder, Dr. Z. Li, Dr. R. S. Ashraf, K. H. Chiu, C.-H. Tan, Prof. J. R. Durrant, Prof. I. McCulloch
Department of Chemistry and Centre for Plastic Electronics
Imperial College London
London, SW7 2AZ, United Kingdom
E-mail: b.schroeder10@imperial.ac.uk, zhe.li@imperial.ac.uk

Dr. J. T. Cabral
Department of Chemical Engineering and Centre for Plastic Electronics
Imperial College London
London, SW7 2AZ, United Kingdom

M. A. Brady, Dr. C. J. Takacs, Prof. M. L. Chabinyc
Materials Department
University of California Santa Barbara
Santa Barbara, California 93106, United States

Dr. G. Faria, D. T. Duong, Prof. A. Salleo
Department of Materials Science and Engineering
Stanford University
476 Lomita Mall, Stanford, California 94305, United States

Keywords: organic solar cell, fullerene, stability, lifetime, PCBM

The power conversion efficiency (PCE) of single junction organic solar cells has increased significantly during the last decade to 9-10%, now approaching the threshold considered necessary to commercialize the technology.[1] During this period, the structural diversity of semiconducting donor polymers for solar cells has increased dramatically.[2] These materials have helped enable an accelerated development of bulk heterojunction (BHJ) organic solar cells based on polymer donor materials and molecular fullerene derivatives. However, the development of electron accepting materials that lead to BHJs with high PCE has been

significantly slower.[3] The most commonly used *n*-type acceptors to date remain [6,6]-phenyl-C_{61}-butyric acid methyl ester ($PC_{61}BM$) and its slightly larger counterpart $PC_{71}BM$.

The morphology of polymer:PCBM BHJs is crucial for optimal PCE; it is important to achieve the "right" trade-off between domain size and finely interconnected network throughout the bulk of the active layer that allows efficient charge generation and extraction. The morphology can be controlled during device fabrication by employing solvent mixtures to deposit the active layer, adding high boiling solvent additives or alternatively by post-deposition treatments like solvent vapor or thermal annealing.[4] However once the active layer is deposited and the desired morphology achieved, it is essential to "lock" that morphology in order to maintain high power efficiencies and to avoid device degradation over time. The "locking" of the active layer morphology is extremely non-trivial, due in part to the fullerene derivatives miscibility in the polymer phase, where they readily diffuse throughout the polymer on short timescales.[5] Over an extended period of time or under thermal stress, the fullerene derivatives, especially $PC_{61}BM$, form micron scale crystallites within the polymer phase acting as charge traps and inhibiting efficient charge transport to the electrodes.[6, 7]

One of the most common approaches to avoid aggregation of fullerenes into large domains is to chemically crosslink either or even both the materials in the BHJ after deposition.[8] Crosslinking, usually triggered by external stimuli (*e.g.* heat or light), has been successfully used in lithography for decades, but proved rather difficult to apply to organic semiconductor thin films. In most cases crosslinking the active layer inadvertently causes a significant performance decrease. We have recently demonstrated a new approach upon which the active layer morphology can be stabilized by the photoinduced [2+2] cycloaddition of the $PC_{61}BM$ derivatives which results in covalent bonding between the fullerene groups.[9] The strategy was found to hold generally for a variety of polymer:fullerene pairs.[7, 10] Light soaking

significantly reduced the formation of $PC_{61}BM$ crystallites under thermal stress and thus the device lifetime subsequently improved. A mechanistic study indicated the enhancement in device thermal stability is primarily associated with inhibition of the nucleation of nanoscale $PC_{61}BM$ aggregates.[7] These observations have motivated us to consider whether enhancement of device stability could also be achieved by the direct addition of covalently linked $PC_{61}BM$ dimers in solution prior to deposition of the active layer. Such an approach could provide a more structurally controlled and robust route to inhibit $PC_{61}BM$ aggregation, as well as enabling direct quantification of the degree of $PC_{61}BM$ dimerization required to enhance device stability, and avoiding limitations associated with thermally induced dissociation observed for photoinduced $PC_{61}BM$ oligomers.[7]

Our synthetic strategy was to make "dumbbell" shaped dimeric fullerenes where the fullerenes are linked via an alkyl bridge between the ester functional group on PCBM. In a first step commercially available **PCBM** was hydrolyzed using a previously described literature procedure and the resulting **PCBA** was recovered as a black soot.[11] The **PCBA** was immediately used in the next reaction step without any further purification. The use of thionyl chloride to convert the **PCBA** into the corresponding acyl chloride was disregarded because thionyl chloride potentially *p*-dopes carbon based molecules like fullerenes, leading ultimately to poor device efficiencies.[12] To prevent this undesired doping, two equivalents of **PCBA** were reacted initially with one equivalent of ethylene glycol under mild reaction conditions using Steglich esterification. Isolating the desired **$(PCB)_2C_2$** dumbbell in sufficient purity from the complex reaction mixture however proved difficult and gave unsatisfactory yields (< 10%). Because of the low solubility of the **PCBA** starting material, it could neither be purified sufficiently prior to reaction nor did it dissolve completely in the employed solvent. As a result, the acid and diol were no longer used in the required stoichiometric ratio, leading to the formation of a variety of compounds, difficult to separate. To circumvent these problems, the

esterification reaction was performed in two steps as shown in **Scheme 1**. The crude **PCBA** was reacted with a large excess of diol (10 equivalents) to encourage the formation of **$PCBC_2OH$**. The highly soluble **$PCBC_2OH$** intermediate was readily purified by column chromatography and recovered in good yields. After a second esterification between **$PCBC_2OH$** and **PCBA**, the **$(PCB)_2C_2$** dumbbell could be successfully assembled and isolated in reasonable yield and excellent purity as evidenced by the ^{1}H-NMR and MALDI spectra shown in **Figure 1**. The singlet associated with the terminal methyl protons in **PCBM** appears at 3.67 ppm, whereas the singlet of the bridging methylene protons in **$(PCB)_2C_2$** are shifted towards lower fields and appear at 4.26 ppm. All remaining signals associated with the aromatic and alkyl protons are identical in both cases and confirm that our dimerization approach has no effect on the chemical environment of the fullerenes.

Because our goal was to blend the dimeric fullerenes with **PCBM**, we investigated the impact of the dimerization on their electronic structure. There have been numerous approaches to synthesize covalently bound fullerene dimers, however most of these synthetic procedures also modify the frontier energy levels of the fullerene dumbbells.[13] In this perspective our controlled dimerization approach is advantageous, allowing the synthesis of structurally well-defined PCBM dumbbells with similar frontier energy levels to **PCBM**, according to density functional theory (DFT) calculations performed at the B3LYP/6-31G* level of theory. The calculations predicted similar HOMO and LUMO energy levels for both **PCBM** and the **$(PCB)_2C_2$** dumbbell and are summarized in **Table 1**. Cyclic voltammetry (CV) measurements were carried out on **PCBM** and **$(PCB)_2C_2$** solutions in *o*-dichlorobenzene and the HOMO and LUMO energy levels were estimated from the onset of the oxidation and reduction (**Figure S10**). In both cases the HOMO was estimated at -5.94 eV and the LUMO at -3.85 eV, thus confirming the trend predicted by DFT calculations. The result might seem intuitive, but ensuring similar energy levels for both **PCBM** and the dimer **$(PCB)_2C_2$** is crucial in order to

achieve high PCE. In case the LUMO energy level of the dimer would be significantly lower than the one of **PCBM**, the added dimer would act as a charge trap, which would be detrimental for device performance.

The UV-*vis.* absorption spectra of both fullerene derivatives were recorded in dilute THF solutions and are shown in **Figure S11**. The fullerene dumbbell shows identical absorption bands to **PCBM** indicating that even though the C_{60} cages are in close proximity due to the covalent ethyl bridge between them, they are not undergoing any additional electronic coupling. This is also supported by quantum mechanical calculations revealing that the both HOMO and LUMO wave function distributions are located on the C_{60} part of the dimer and are not affected by the ethyl linkage (**Figure S12**).

To investigate the effect of addition of **$(PCB)_2C_2$** on the active layer morphology and device performance, a blend of **PCBM** with the carbazole based **PCDTBT** polymer was chosen as model system. **PCDTBT** is a high performing amorphous polymer with a glass transition temperature ($T_g \approx 106°C$) in neat films below the temperatures used here for examination of thermal stability.[14] To determine the minimum weight percentage of **$(PCB)_2C_2$** dumbbell necessary to stabilize the **PCDTBT:PCBM** blend under thermal stress, blends of **PCDTBT**:fullerene (1:2) were spin coated on silicon substrates from chlorobenzene and thermally annealed at 140°C for 1 hour. We have studied the effect of dimer content in the fullerene component, while maintaining the overall weight ratio of polymer:fullerene constant. From the optical micrographs presented in **Figure S13**, it is apparent that the addition of dimer leads to a more thermally stable blend. At low dimer loadings (< 1% by mass) the growth of micron sized **PCBM** crystallites in the blend cannot be inhibited. However, the formation of micron-sized **PCBM** crystallites at temperatures above the T_g of the pure polymer is completely impeded upon addition of 20% of **$(PCB)_2C_2$** (**Figure 2**), and indeed the number density of the **PCBM** crystallites is suppressed by over 50% by adding only 5% of

dimer to the blend (**Figure 3A**). This low threshold is consistent with our previous conclusion that the primary role of the $PC_{61}BM$ oligomers, respectively **$(PCB)_2C_2$**, is to frustrate and eventually inhibit $PC_{61}BM$ crystal nucleation, with such nucleation processes often being hindered by low compositions of additive materials.[7, 15]

The effect of **$(PCB)_2C_2$** on the nanomorphological behavior upon thermal stress analogous to solar cell operating conditions was also investigated. Our previous studies have shown that thermal stress at temperatures relevant to device operation does not lead to micron-size crystallites, but instead results in the formation of nanometer-sized **PCBM** features in **PCDTBT:PCBM** blend films instead.[7] The evolution of the blend morphology upon thermal annealing at 85°C, customary for standard thermal stress tests, on PEDOT:PSS substrates is shown in **Figure 2**.[16] As revealed by AFM, as cast samples are relatively smooth and featureless, with a similar surface roughness for both with and without **$(PCB)_2C_2$**. Upon thermal annealing at 85°C for 1 h, the samples without **$(PCB)_2C_2$** exhibit densely formed **PCBM** crystallites of the order of 150 nm in diameter and 30 nm in height. We have previously assigned these nanoscale features to **PCBM** aggregates, and correlated their appearance with the degradation of device efficiency under modest thermal stress.[7] In clear contrast, the samples with 20% **$(PCB)_2C_2$** show drastically suppressed **PCBM** aggregation with no measurable change in film surface morphology after thermal treatment.

The film morphology was further probed by bright field transmission microscopy (TEM). At 80°C, both blend films, with and without **$(PCB)_2C_2$**, present very comparable features. The non-**$(PCB)_2C_2$** containing blend contains spherical aggregates dispersed homogenously throughout the film (**Figure S14** to **S16**), with diameters ranging from ~150-250 nm. The **$(PCB)_2C_2$** containing blend showed comparable features, but a much lower density of fullerene nuclei of approximate diameter of ~100-150 nm was found. This modest difference suggests that the observed spherical aggregates in the non-**$(PCB)_2C_2$** containing blend might

play a key role in **PCBM** crystal nucleation and device degradation even though the exact mechanism is not yet elucidated. Upon thermal annealing at 140°C, the formation of fullerene nuclei varying in size (~50-100, 100-150 and 150-200 nm) was observed in the non-**$(PCB)_2C_2$** containing blend. More importantly however, we observed the formation of needle-like structures, similar to the ones previously observed in optical microscopy image, but much smaller in size (50-100 nm in length and 10 nm in width). In the annealed blend film containing 20% of **$(PCB)_2C_2$** these sheaf-like structures were not observed, but the morphology was instead characterized by the presence of spherical aggregates, on average smaller than the ones observed prior to 140°C annealing. These results are in further agreement with our previously made observation that a low concentration of **$(PCB)_2C_2$** in the fullerene phase is stabilizing the blend nano morphology and seems to influence the shape and number density of **PCBM** aggregates under modest thermal stress.

Knowing that the **PCBM** dumbbell has a positive effect on the thermal stability of active layer blend films, we focused on its effect on the performance of **PCDTBT:PCBM** solar cells. A standardized thermal stress of 85°C was applied to the devices under nitrogen atmosphere, with the current-voltage (J-V) recorded using repeated dark thermal annealing/room temperature device testing cycles. For J-V measurements, devices were exposed under a solar simulator for less than 30 seconds during each measurement to minimize the effect of **PCBM** photo-oligomerisation. **Figure 3** demonstrates the impact of a low percentage of **PCBM** dimers on the efficiency and thermal stability of **PCDTBT:PCBM** devices. Devices containing 20% of **$(PCB)_2C_2$** show a modest improvement in efficiency compared to devices without dimers, primarily due to an enhancement in fill factor (FF) from around 0.56 to 0.62. The cause of improved FF is not obvious from the AFM images e) and f) in **Figure 2**, but is likely due to an improvement in the blend morphology induced by the dimers during film deposition. For the devices fabricated without **$(PCB)_2C_2$**, a rapid degradation in device

performance was observed upon thermal stress, with a 20% loss in power conversion efficiency (PCE) within the first 25 minutes, primarily due a loss of fill factor, and likely linked to the densely formed nanoscale **PCBM** aggregates. Remarkably, devices containing 20% of the **$(PCB)_2C_2$** show significantly improved thermal device stability with a reduction in the PCE by 20% occurring only after 2000 minutes. It is thus apparent that the device thermal stability of conventional **PCDTBT:PCBM** devices can be enhanced by an order of magnitude by using a low percentage of **$(PCB)_2C_2$**, at least under the thermal stress conditions and time scale studied herein.

Given that the addition of **$(PCB)_2C_2$** not only enhances long term device stability, but also device efficiency, we evaluated the potential to further enhance device performance by systematically increasing the **PCBM** dimer loading from 0% (100% of **PCBM**) to 100% (0% of **PCBM**) while keeping the total concentration of fullerene in the active layer blend constant. The initial device J-V characteristics, as a function of the **$(PCB)_2C_2$** loading, are shown in **Figure S17**. From 0% to 20% of **$(PCB)_2C_2$** loading, modest increases in PCE are observed due to enhanced FF values. However, further increase in dimer loading results in decreasing device PCE, caused by decreases in both J_{sc} and FF (See **Table S1** in supporting information for detailed device parameters). The loss in PCE results in part from a higher series resistance, indicative of a drop in electron mobility in the fullerene phase with increasing **PCBM** dimer loading. To confirm this assumption, organic field effect transistors (OFET) were built to measure the electron mobility as a function of **$(PCB)_2C_2$** loading. The electron mobility of a neat **PCBM** film was found to be around 1×10^{-3} $cm^2V^{-1}s^{-1}$, which is in good agreement with previously reported literature values.[17] As evidenced from **Figure 4**, a sharp drop in electron mobility is observed at **$(PCB)_2C_2$** loadings exceeding 10-20%, which correlates well with the lower J_{sc} measured at higher dumbbell loadings and the resulting drop in PCE. These findings are in line with previous work by Distler *et al.*, [18] who demonstrated that photodimerisation

of **PCBM** causes a significant reduction of charge carrier mobility in a polymer:fullerene system, resulting in a reversible degradation of device efficiency under constant illumination. The electron mobility measurements in conjunction with the device stability data therefore conclusively show that there is an optimal **$(PCB)_2C_2$** loading around 20% at which both the device efficiency and the device lifetime can be simultaneously enhanced.

Based on the aforementioned results, the addition of **$(PCB)_2C_2$** leads to improved power conversion efficiencies, mainly because the growth of nm-sized **PCBM** crystallites in the active layer under thermal stress is prevented as evidenced by AFM measurements. To further investigate by what mechanism this crystallite growth is suppressed, we have carried out interdiffusion measurements. We hypothesized above that the addition of **$(PCB)_2C_2$** would lead to lower fullerene diffusion coefficients, thus slowing down and eventually preventing, the growth of **PCBM** nanocrystallites. The diffusion of **$(PCB)_2C_2$** from a bulk heterojunction blend with **PCDTBT** into a neat **PCDTBT** thin film was thus investigated with dynamic secondary ion mass spectrometry as a function of annealing temperature (**Figure 5**). The bilayers remained stable in composition, as prepared from solution casting and film lamination, until the annealing temperature approached the T_g of **PCDTBT** (beginning at 100°C). At temperatures near or slightly below T_g, the **$(PCB)_2C_2$** infiltrated only partially into the **PCDTBT** film, with a decreasing dimer concentration with diffusion distance. At temperatures above T_g, the **$(PCB)_2C_2$** diffused entirely across the **PCDTBT** film with uniform concentration. These results suggest that the molecular mobility of **PCDTBT** is critical in determining the ability for the dimer molecule to traverse the polymer phase. While **$(PCB)_2C_2$** and **PCBM** show qualitatively the same behavior with **PCDTBT**, we cannot rule out that the diffusion of the former is slowed down, as the DSIMS measurement provides only a bound for the diffusion constant. We can state however that it is not slowed so much as to retard diffusion at timescales commonly used in processing of BHJs, i.e. ~minutes. More critically,

the miscibility in **PCDTBT** seems unaffected by the dimerization process. These results imply that in blends with **PCDTBT**, dimerized and undimerized **PCBM** show similar diffusion kinetics and suggest that rather than slowing growth of domains by mass diffusion in such blends, that the stability of the microstructure is achieved through frustration of molecular packing of **PCBM** by **$(PCB)_2C_2$**. Grazing incidence wide angle x-ray scattering (GIWAXS) measurements performed on **PCDTBT**:fullerene blends revealed only some weak ordering from **PCDTBT**, with (100) and (200) peaks that are broad and weakly observable in the out-of-plane and in-plane directions (**Figure 6**). The large, broad aggregate peak centered at ~1.4 $Å^{-1}$ has contributions from the weakly ordered/aggregated **PCBM** and possibly **$(PCB)_2C_2$**, as well as from the amorphous regions of **PCDTBT**. No diffraction peaks related to the spherical fullerene aggregates observed in TEM images could be identified, which is likely because these are very weakly ordered.

The hypothesis of frustrated molecular packing is further supported by differential scanning calorimetric (DSC) measurements as evidenced from **Figure S18-S22**. Pure **PCBM** exhibits a sharp melting peak at 280°C with an associated enthalpy of fusion of 14.8 J/g. However upon addition of 20% of **$(PCB)_2C_2$** dumbbell, it is possible to quench the **PCBM:$(PCB)_2C_2$** blend in a glassy state ($T_g \approx 200°C$) and even after 2 hours of thermal annealing at 85°C the sample did not return to a crystalline state comparable to the neat **PCBM** sample (**Figure 6C**).

These results demonstrate conclusively that the addition of a modified fullerene to a polymer:fullerene active layer does not negatively affect the PCE of BHJs and can lead to the significantly enhanced morphological stability. The underlying mechanism appears to be, not a significant reduction in fullerene mobility, but rather the frustration of fullerene nanocrystal nucleation. We find that there is an optimal loading, of approximately 20% fullerene dimer, that yields a device lifetime increase of around 20% under realistic operating conditions. In contrast with our previously reported strategy of photo-induced fullerene oligomerisation in

the active layer, which yields a time-dependent fullerene:oligomer population (as a function of time and illumination), this approach is robust to environmental conditions and thus potentially more attractive for practical implementation.

Supporting Information

Supporting Information is available from the Wiley Online Library or from the authors.

Acknowledgements

The authors would like to acknowledge the Imperial College High Performance Computing Service for providing the computing facilities to perform the quantum-mechanical calculations. BCS gratefully acknowledges funding from the EPSRC knowledge transfer secondment scheme. Financial support from Solvay SA is grateful acknowledged. This work was in part carried out under the EPSRC Projects EP/F056710/1, EP/I019278/1 and EP/G037515/1 with support from the Centre for Plastic Electronics at Imperial. MLC and MAB were partially funded by NSF CHE ICC award 1026664. Thanks to Christine Schroeder-Schanck for designing the TOC graphic.

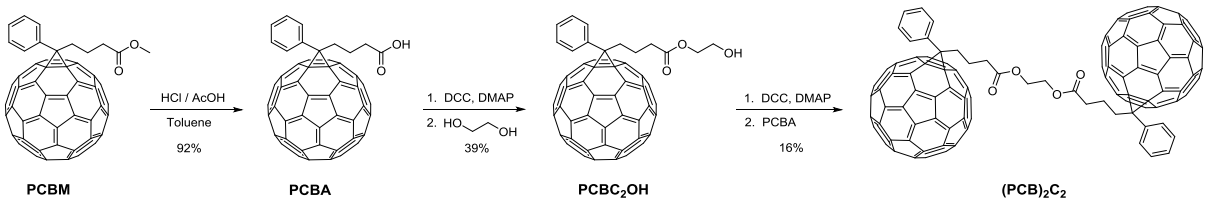
Received: ((will be filled in by the editorial staff))
Revised: ((will be filled in by the editorial staff))
Published online: ((will be filled in by the editorial staff))

[1] J. You, L. Dou, K. Yoshimura, T. Kato, K. Ohya, T. Moriarty, K. Emery, C.-C. Chen, J. Gao, G. Li, Y. Yang, Nature Communications 2013, 4, 1446; W. Li, A. Furlan, K. H. Hendriks, M. M. Wienk, R. A. J. Janssen, Journal of the American Chemical Society 2013, 135, 5529; T. Ameri, N. Li, C. J. Brabec, Energy & Environmental Science 2013, 6, 2390; M. C. Scharber, N. S. Sariciftci, Progress in Polymer Science 2013, 38, 1929.
[2] A. Facchetti, Chemistry of Materials 2010, 23, 733; C. L. Chochos, S. A. Choulis, Progress in Polymer Science 2011, 36, 1326; A. Pron, M. Leclerc, Progress in Polymer Science 2013, 38, 1815.
[3] P. Sonar, J. P. Fong Lim, K. L. Chan, Energy & Environmental Science 2011, 4, 1558; C. L. Chochos, N. Tagmatarchis, V. G. Gregoriou, RSC Advances 2013, 3, 7160; K. N. Winzenberg, P. Kemppinen, F. H. Scholes, G. E. Collis, Y. Shu, T. Birendra Singh, A. Bilic, C. M. Forsyth, S. E. Watkins, Chemical Communications 2013, 49, 6307; A. Sharenko, C. M.

Proctor, T. S. van der Poll, Z. B. Henson, T.-Q. Nguyen, G. C. Bazan, Advanced Materials 2013, 25, 4403.
[4] G. Li, Y. Yao, H. Yang, V. Shrotriya, G. Yang, Y. Yang, Advanced Functional Materials 2007, 17, 1636; J. K. Lee, W. L. Ma, C. J. Brabec, J. Yuen, J. S. Moon, J. Y. Kim, K. Lee, G. C. Bazan, A. J. Heeger, Journal of the American Chemical Society 2008, 130, 3619; J. H. Park, J. S. Kim, J. H. Lee, W. H. Lee, K. Cho, The Journal of Physical Chemistry C 2009, 113, 17579; E. Verploegen, R. Mondal, C. J. Bettinger, S. Sok, M. F. Toney, Z. Bao, Advanced Functional Materials 2010, 20, 3519.
[5] N. D. Treat, M. A. Brady, G. Smith, M. F. Toney, E. J. Kramer, C. J. Hawker, M. L. Chabinyc, Advanced Energy Materials 2011, 1, 82.
[6] S. Ebadian, B. Gholamkhass, S. Shambayati, S. Holdcroft, P. Servati, Solar Energy Materials and Solar Cells 2010, 94, 2258; T. Wang, A. J. Pearson, A. D. F. Dunbar, P. A. Staniec, D. C. Watters, H. Yi, A. J. Ryan, R. A. L. Jones, A. Iraqi, D. G. Lidzey, Advanced Functional Materials 2012, 22, 1399.
[7] H. C. Wong, Z. Li, C. H. Tan, H. Zhong, Z. Huang, H. Bronstein, I. McCulloch, J. T. Cabral, J. R. Durrant, ACS Nano 2014, 8, 1297.
[8] Y.-J. Cheng, C.-H. Hsieh, P.-J. Li, C.-S. Hsu, Advanced Functional Materials 2011, 21, 1723; C.-Y. Nam, Y. Qin, Y. S. Park, H. Hlaing, X. Lu, B. M. Ocko, C. T. Black, R. B. Grubbs, Macromolecules 2012, 45, 2338; G. Wantz, L. Derue, O. Dautel, A. Rivaton, P. Hudhomme, C. Dagron-Lartigau, Polymer International 2014, n/a.
[9] Z. Li, H. C. Wong, Z. Huang, H. Zhong, C. H. Tan, W. C. Tsoi, J. S. Kim, J. R. Durrant, J. T. Cabral, Nat Commun 2013, 4.
[10] F. Piersimoni, G. Degutis, S. Bertho, K. Vandewal, D. Spoltore, T. Vangerven, J. Drijkoningen, M. K. Van Bael, A. Hardy, J. D'Haen, W. Maes, D. Vanderzande, M. Nesladek, J. Manca, Journal of Polymer Science Part B: Polymer Physics 2013, 51, 1209; H. C. Wong, A. M. Higgins, A. R. Wildes, J. F. Douglas, J. T. Cabral, Advanced Materials 2013, 25, 985.
[11] Q. Wei, T. Nishizawa, K. Tajima, K. Hashimoto, Advanced Materials 2008, 20, 2211.
[12] U. Dettlaff-Weglikowska, V. Skákalová, R. Graupner, S. H. Jhang, B. H. Kim, H. J. Lee, L. Ley, Y. W. Park, S. Berber, D. Tománek, S. Roth, Journal of the American Chemical Society 2005, 127, 5125.
[13] J. L. Segura, N. Martin, Chemical Society Reviews 2000, 29, 13; S. R. Plant, M. Jevric, J. J. L. Morton, A. Ardavan, A. N. Khlobystov, G. A. D. Briggs, K. Porfyrakis, Chemical Science 2013, 4, 2971; A. La Rosa, K. Gillemot, E. Leary, C. Evangeli, M. T. González, S. Filippone, G. Rubio-Bollinger, N. Agraït, C. J. Lambert, N. Martín, The Journal of Organic Chemistry 2014.
[14] N. Blouin, A. Michaud, M. Leclerc, Advanced Materials 2007, 19, 2295.
[15] C. Lindqvist, J. Bergqvist, C.-C. Feng, S. Gustafsson, O. Bäcke, N. D. Treat, C. Bounioux, P. Henriksson, R. Kroon, E. Wang, A. Sanz-Velasco, P. M. Kristiansen, N. Stingelin, E. Olsson, O. Inganäs, M. R. Andersson, C. Müller, Advanced Energy Materials 2014, n/a.
[16] M. O. Reese, S. A. Gevorgyan, M. Jørgensen, E. Bundgaard, S. R. Kurtz, D. S. Ginley, D. C. Olson, M. T. Lloyd, P. Morvillo, E. A. Katz, A. Elschner, O. Haillant, T. R. Currier, V. Shrotriya, M. Hermenau, M. Riede, K. R. Kirov, G. Trimmel, T. Rath, O. Inganäs, F. Zhang, M. Andersson, K. Tvingstedt, M. Lira-Cantu, D. Laird, C. McGuiness, S. Gowrisanker, M. Pannone, M. Xiao, J. Hauch, R. Steim, D. M. DeLongchamp, R. Rösch, H. Hoppe, N. Espinosa, A. Urbina, G. Yaman-Uzunoglu, J.-B. Bonekamp, A. J. J. M. van Breemen, C. Girotto, E. Voroshazi, F. C. Krebs, Solar Energy Materials and Solar Cells 2011, 95, 1253.
[17] T. D. Anthopoulos, D. M. de Leeuw, E. Cantatore, P. van 't Hof, J. Alma, J. C. Hummelen, Journal of Applied Physics 2005, 98; E. von Hauff, V. Dyakonov, J. Parisi, Solar Energy Materials and Solar Cells 2005, 87, 149.

[18] A. Distler, T. Sauermann, H.-J. Egelhaaf, S. Rodman, D. Waller, K.-S. Cheon, M. Lee, D. M. Guldi, Advanced Energy Materials 2014, 4, n/a.

Figures and captions:



Scheme 1. Synthesis of the PCBM dumbbell **$(PCB)_2C_2$**.

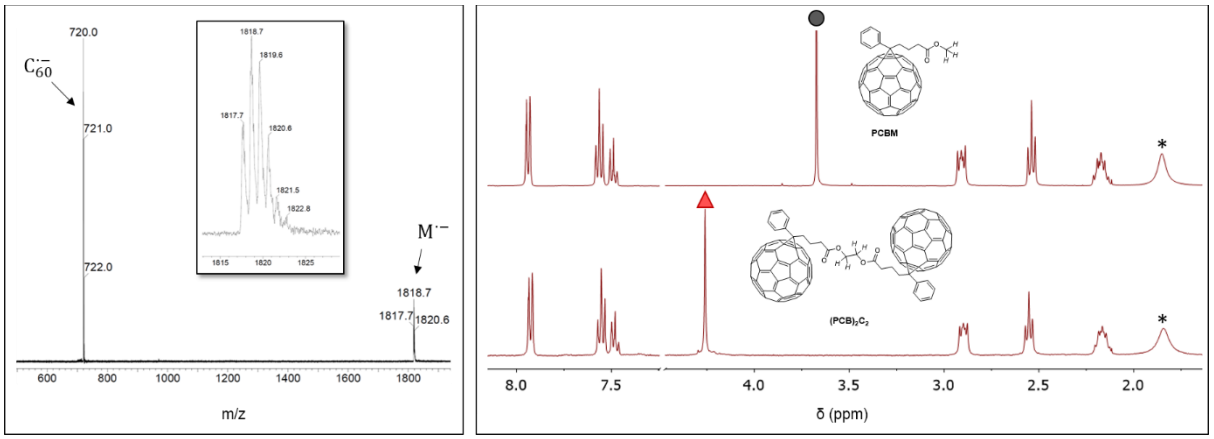


Figure 1. (Left) Negative ion MALDI mass spectrum of **$(PCB)_2C_2$**, using C_{60} (m/z: 720.0) as internal calibrant. The inset shows a zoomed view of the molecular ion peak. (Right) ^{1}H-NMR spectra of **PCBM** (top) and **$(PCB)_2C_2$** (bottom) recorded at 293 K in 1,1,2,2-tetrachloroethane-d_2. In the **PCBM** spectrum, the singlet attributed to the terminal methyl protons is highlighted with a black circle. Similarly the singlet assigned to the bridging methylene protons in the **$(PCB)_2C_2$** spectrum are marked by a red triangle. The broad peak at 1.84 ppm (marked by a *) originates from residual water in the NMR solvent.

Table 1. Electrochemical, theoretical and optical properties of **PCBM** and **$(PCB)_2C_2$**.

	CV	DFT	UV-vis.
Compound	HOMO/LUMO [eV] [a]	HOMO/LUMO [eV] [b]	λ_{max} soln. [nm] [c]
PCBM	-5.94 / -3.85	-5.70 / -3.13	258, 328
$(PCB)_2C_2$	-5.94 / -3.85	-5.71 / -3.14	258, 328

[a] Measured in *o*-dichlorobenzene solution with 0.1 M $TBAPF_6$ as supporting electrolyte. Scan rate 100 mV/s. [b] Energy levels calculated by DFT using the B3LYP/6-31g* model. [c] Recorded in dilute THF solution at 25°C.

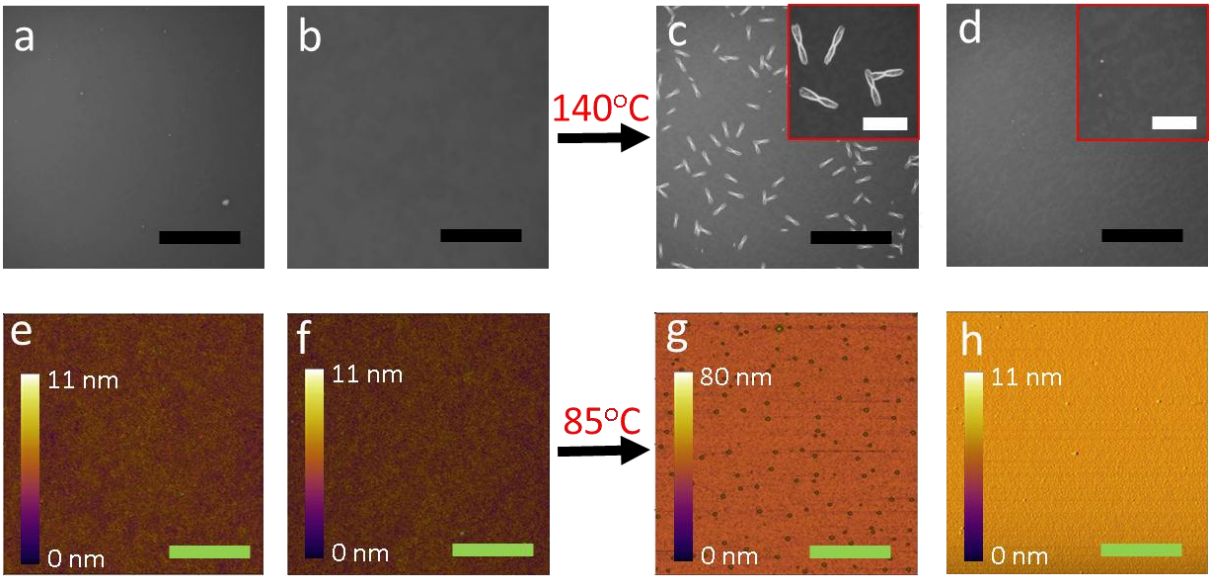


Figure 2. Optical images of a) **PCDTBT:PCBM** as-cast blend films; b) **PCDTBT:PCBM:$(PCB)_2C_2$** (20%) as-cast films; c) **PCDTBT:PCBM** blend films after thermal annealing at 140°C for 1h and d) **PCDTBT:PCBM:$(PCB)_2C_2$** (20%) blend films after thermal annealing at 140°C for 1h on SiO_x substrates (scale bar, 200 µm). The insets c) and d) highlight the drastic differences in **PCBM** crystal formation in the annealed blend films with and without the **$(PCB)_2C_2$** (scale bar is 40 µm). AFM images of e) **PCDTBT:PCBM** as-cast blend films; f) **PCDTBT:PCBM:$(PCB)_2C_2$** (20%) as-cast films; g) **PCDTBT:PCBM** blend films after thermal annealing at 85°C for 1h; and h)

PCDTBT:PCBM:$(PCB)_2C_2$ (20%) blend films after thermal annealing at 85°C for 1h on PEDOT:PSS substrates (scale bar is 5.7 μm).

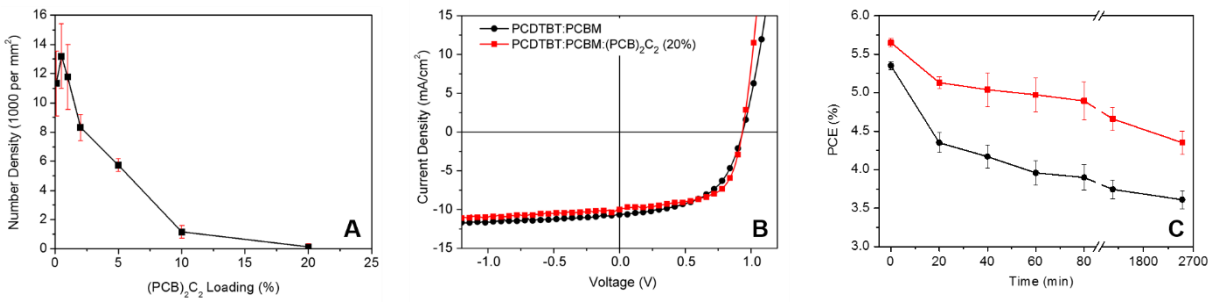


Figure 3. (A) Number density of micron sized **PCBM** crystallites formed in blend films after thermal annealing at 140°C for 1h on SiO_x/Si substrates, plotted as a function of **$(PCB)_2C_2$** dimer loading. (B) Comparison of the J-V characteristics of optimized conventional **PCDTBT:PCBM** devices and **PCDTBT:PCBM:$(PCB)_2C_2$** (20%). (C) Degradation of solar cell PCE as a function of annealing time at 85°C in nitrogen atmosphere. The error bars represent the spread in degradation kinetics of three typical devices.

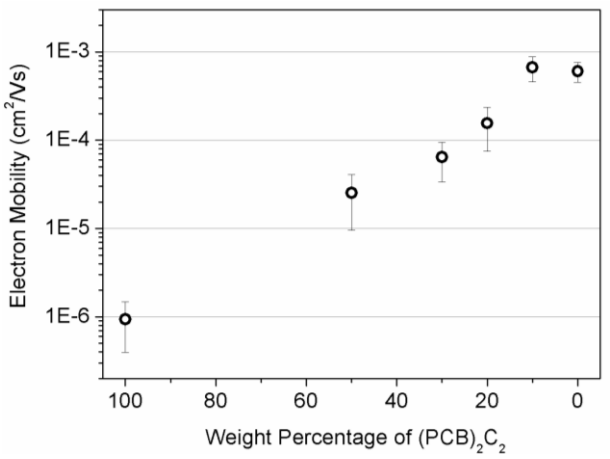


Figure 4. Electron mobility of **PCBM:$(PCB)_2C_2$** measured in organic field effect transistors as a function of **$(PCB)_2C_2$** loading.

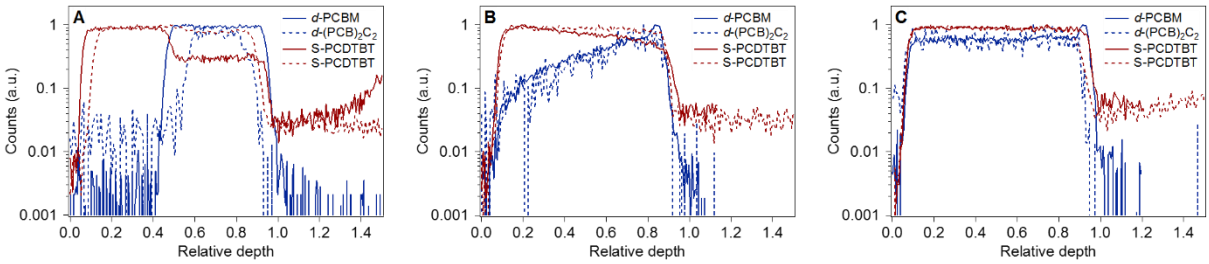


Figure 5. DSIMS profiles of ^{2}H and ^{32}S in a **PCDTBT:*d*-PCBM** bilayer (solid lines) and in a **PCDTBT:**(BHJ **PCDTBT:*d*-(PCB)$_2$C$_2$**) bilayer (dotted line) fabricated on a SiO_2/Si substrate. (A) Sharp changes in the ^{2}H and ^{32}S counts are observed in the as-cast bilayer structures. (B) Partial infiltration of the deuterated fullerene derivatives into the **PCDTBT** layers occurs at 100°C annealing and (C) homogenous distributions of the deuterated species is achieved at an annealing temperature (140°C) exceeding the polymers T_g.

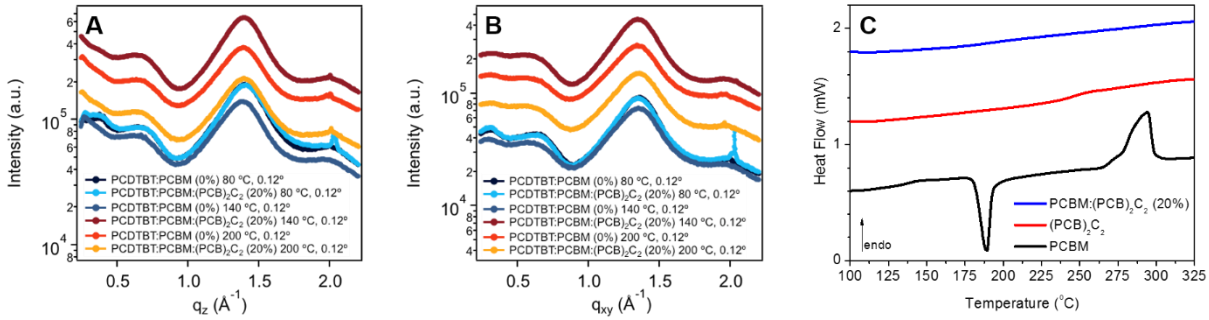


Figure 6. (A) out-of-plane and (B) in-plane GIWAXS diffraction patterns of **PCDTBT:PCBM** and **PCDTBT:PCBM:(PCB)$_2$C$_2$** (20%) BHJ films, annealed at various temperatures prior to the measurements; (C) DSC first heating thermogram of **PCBM**, **(PCB)$_2$C$_2$** and **PCBM:(PCB)$_2$C$_2$** (20%) after the samples were thermally annealed at 85°C during two hours. Heating rate 10°C/min.

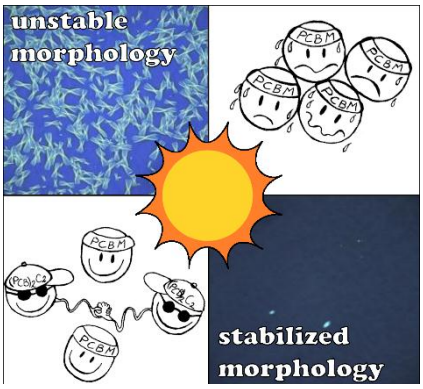
The table of contents entry

Long term operational stability of organic photovoltaics remains a challenge, especially at elevated temperatures. Herein we present the synthesis of a fullerene dumbbell and its use as an additive in the active layer. The addition of the dumbbell not only leads to improved device efficiencies, but more importantly also to a dramatic increase in morphological stability under simulated operating conditions.

Keywords: organic solar cell, fullerene, stability, lifetime, PCBM

Bob C. Schroeder,* Zhe Li,* Michael A. Brady, Gregório Faria, Raja Shahid Ashraf, Christopher J. Takacs, Duc T. Duong, Kar Ho Chiu, Ching-Hong Tan, João T. Cabral, Alberto Salleo, Michael L. Chabinyc, James R. Durrant, and Iain McCulloch

Enhancing fullerene-based solar cell lifetimes by addition of a fullerene dumbbell



Copyright WILEY-VCH Verlag GmbH & Co. KGaA, 69469 Weinheim, Germany, 2013.

Supporting Information

Enhancing fullerene-based solar cell lifetimes by addition of a fullerene dumbbell

Bob C. Schroeder, Zhe Li,* Michael A. Brady, Gregório Faria, Raja Shahid Ashraf, Christopher J. Takacs, Duc T. Duog, Kar Ho Chiu, Ching-Hong Tan, João T. Cabral, Alberto Salleo, Michael L. Chabinyc, James R. Durrant, and Iain McCulloch*

Experimental details	X
Synthetic details	X
Cyclic voltammetry, UV-vis. absorption and computational data	X
Microscopy and TEM images	X
OPV data	X
DSC traces	X
OFET transfer and output curves	X

PCBM was purchased from Solenne BV, all other chemicals and solvents were purchased from Sigma-Aldrich and used as received. **PCBA** was synthesized according to a literature procedure. [11] ^{1}H NMR and ^{13}C NMR spectra were recorded on a Bruker 400 spectrometer at 298 K and chemical shifts are given in ppm. UV-*vis.* absorption spectra were recorded on a UV-1800 Shimadzu UV-*vis*. spectrometer. Cyclic voltammograms were obtained using an Autolab PGSTAT101 potentiostat with a standard three-electrode setup with a platinum disk working electrode and a Ag/Ag^{+} reference electrode calibrated against Fc/Fc^{+}. The measurements were carried out with approximately 0.5 $\times 10^{-3}$ M solutions of **PCBM**, respectively **$(PCB)_2C_2$**, in a mixture of anhydrous and deoxygenated acetonitrile:*o*-dichlorobenzene (1:5 v/v) with 0.1 M tetrabutylammonium hexafluorophosphate as the supporting electrolyte at a scan rate of 100 mV/s. HOMO and LUMO energy values were obtained using equations:

$$E_{LUMO} = -(E_{red} - E_{Fc} + 4.8)\ \text{eV and}\ E_{HOMO} = -(E_{ox} - E_{Fc} + 4.8)\ \text{eV}$$

PCDBT was supplied by 1-Materials Inc. ($M_w \approx 21.6$ kg.mol^{-1}; $D_w \approx 5.5$) and **PCBM** was purchased from Nano-C Inc. **PCDTBT** and **PCBM**, respectively **$(PCB)_2C_2$**, (1:2 weight ratio) were co-dissolved in chlorobenzene and stirred for 24 hours at 55°C inside a nitrogen filled glovebox. The total solution concentration was 25 mg.mL^{-1}. All devices were prepared with a conventional device architecture (ITO/PEDOT:PSS/PCDTBT:PCBM/Ca/Al), the active layer was deposited via spincoating at room temperature and the film thickness was measured to be around 80 nm.

Matrix-assisted laser desorption ionization (MALDI) mass spectra (MS) were obtained using a Micromass MALDI mass spectrometer equipped with a time-of-flight (ToF) analyzer. All mass spectra were acquired in negative mode. *trans*-2-[3-(4-*tert*-Butylphenyl)-2-methyl-2-propenylidene]malononitrile was used matrix. The sample was deposited together with the

matrix and C_{60} as internal reference from *o*-dichlorobenzene solution by drop-casting directly on the MALDI plate. mode.

DSC experiments were carried out with a TA Instruments DSC Q20. The samples for the thermal annealing DSC measurements, were prepared by loading the DSC pan with the analyte and heating the sample multiple times to 325°C and until consecutive heating cycles were identical. The sample was then annealed at 85°C during two hours in the DSC machine and heated to 325°C to induce the melt. Atomic force miscroscopy (AFM) was performed using an Asylum Research MFP 3D AFM, using NanoWorld Pointprobe Al-coated, non-contacted mode Si cantilevers, with a resonance frequency of 190 kHz and a spring constant of 48 N/m.

Dynamic secondary ion mass spectrometry (SIMS) was performed using a Physical Electronics 6650 quadropole instrument. Substrates were cooled on a cryostage (liquid nitrogen) for ~30 min prior to measurement. A 2kV O_2^+ beam at ~40-50 nA was rastered across a 300 μm x 300 μm area, of which only the middle 15% of the surface area was analyzed for composition through collection of negative secondary ions.

2D GIWAXS was conducted at beamline 7.3.3 at the Advanced Light Source (Lawrence Berkeley National Laboratory), using a Pilatus 1M CCD detector at grazing incidence with a photon energy of 10 keV. Samples were kept under helium atmosphere to minimize sample radiation damage and the low-q background in the collected images. Films were typically exposed for 60-90 s at incident angles of 0.10-0.18°.

OFET SI

[6,6]-Phenyl-C61-butyric acid 2-hydroxyethyl ester ($PCBC_2OH$). [6,6]-Phenyl-C61-butyric acid (**PCBA**) (600 mg, 0.67 mmol) was added to 100 mL of anhydrous *o*-dichlorobenzene and sonicated during 20 minutes. After sonication the brownish suspension was heated to 110°C for two hours in order to fully dissolve the PCBA. The resulting black solution was cooled to 0°C in an ice-bath before ethylene glycol (1 mL, 17.88 mmol) and 4-Dimethylaminopyridine (8.2 mg, 0.07 mmol) were added. At last *N*,*N*'-Dicyclohexylcarbodiimide (152 mg, 0.74 mmol) was added to the reaction mixture, which was allowed to warm to room temperature and stirred overnight. The solvent was removed from the reaction mixture by rotary evaporation. The recovered crude product was purified by column chromatography on silica gel using a mixture of toluene:pyridine (95:5) as mobile phase. The recovered fractions were concentrated and precipitated into cold methanol. The title compound was recovered as a brown solid after filtration (247 mg, 0.26 mmol, 39%). ^{1}H NMR (400 MHz, chloroform-*d*) δ ppm 7.97 - 7.91 (m, 2 H) 7.60 - 7.46 (m, 3 H) 4.27 - 4.21 (m, 2 H) 3.88 - 3.77 (m, 2 H) 3.01 – 2.87 (m, 2 H) 2.59 (t, *J*=7.3 Hz, 2 H) 2.29 - 2.15 (m, 2 H) 1.80 (br s, 1 H). MS (MALDI-ToF): *m/z* calcd for $C_{73}H_{16}O_3$ ($M^{\cdot-}$) 940.1, 941.1, 942.1, 943.1 found 940.1, 941.1, 942.1, 943.1.

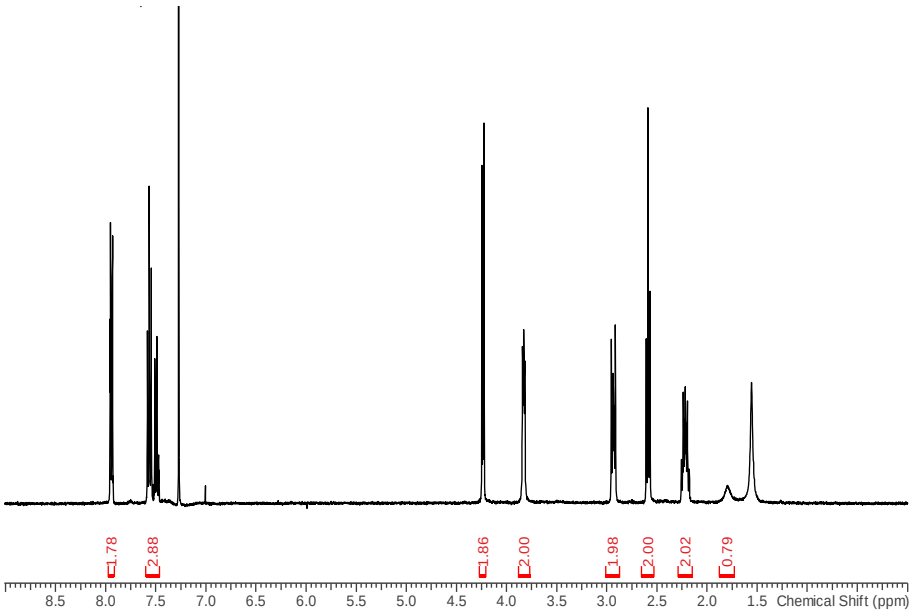


Figure S1. [1]H-NMR spectra of **$PCBC_2OH$** recorded at 293 K in chloroform-*d*.

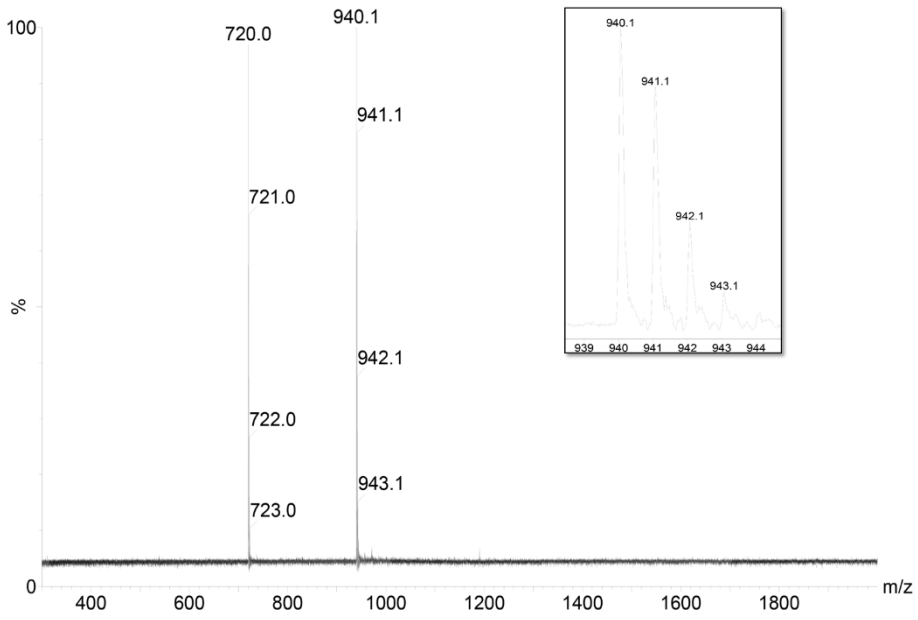


Figure S2. Negative ion MALDI mass spectrum of **$PCBC_2OH$**, using C_{60} (m/z: 720.0) as internal calibrant. The inset shows a zoomed view of the molecular ion peak.

Bis-[6,6]-phenyl-C61-butyric acid ethane-1,2-diyl ester ($(PCB)_2C_2$).

$PCBC_2OH$ (190 mg, 0.20 mmol) was dissolved in 100 mL of anhydrous *o*-dichlorobenze and cooled to 0°C. PCBA (362 mg, 0.40 mmol) and 4-Dimethylaminopyridine (4.9 mg, 0.04 mmol) were added, before *N*,*N'*-Dicyclohexylcarbodiimide (92 mg, 0.44 mmol) was added. The reaction mixture was allowed to warm to room temperature and stirred overnight. Afterwards the solvent was removed from the reaction mixture and the recovered crude product was purified by column chromatography on silica gel using toluene as eluent. The recovered fractions were concentrated and precipitated into methanol. The title compound was recovered as a dark brown solid after filtration (58 mg, 0.03 mmol, 16%). [1]H NMR (400 MHz, 1,1,2,2-tetrachloroethane-d_2) δ ppm 7.91 - 7. 86 (m, 2 H) 7.55 - 7.42 (m, 3 H) 4.22 (s, 2 H) 2.91 – 2.80 (m, 2 H) 2.51 (t, *J*=7.3 Hz, 2 H) 2.18 -1.94 (m, 2 H). [13]C NMR (100 MHz,

TCE-d_2) δ ppm 207.5, 173.2, 149.0, 148.0, 146.1, 145.4, 145.4, 145.3, 145.2, 145.0, 144.9, 144.7, 144.6, 144.2, 144.0, 143.2, 143.2, 143.1, 142.4, 142.4, 142.3, 141.2, 140.9, 138.2, 137.8, 136.9, 136.5, 132.3, 128.8, 128.5, 123.8, 120.6, 80.1, 52.1, 34.1, 33.8, 22.5. MS (MALDI-ToF): *m/z* calcd for $C_{144}H_{26}O_4$ ($M^{\cdot-}$) 1819.2, 1820.2, 1818.2, 1821.2 found 1818.7, 1819.6, 1817.7, 1820.6.

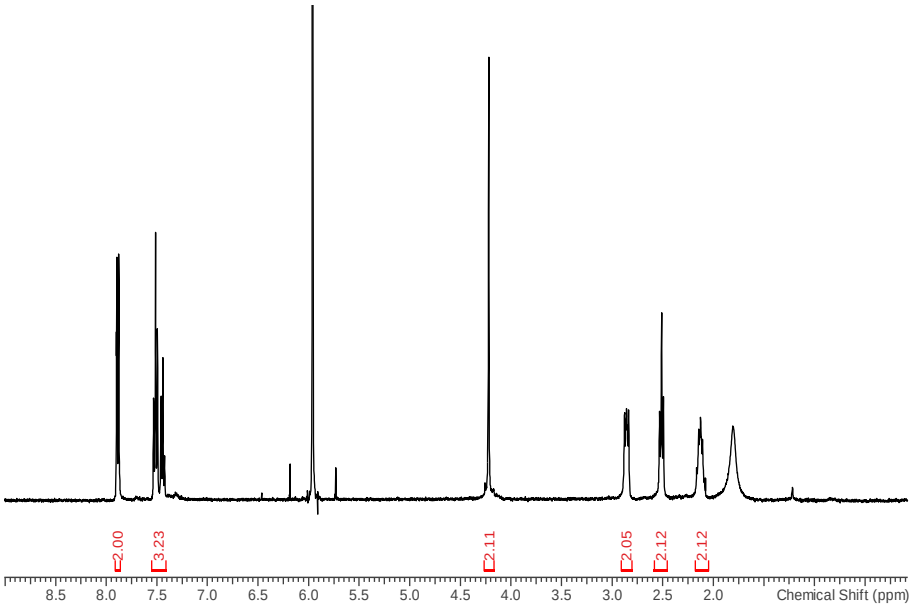


Figure S3. ^{1}H-NMR spectra of **(PCB)$_2$C$_2$** recorded at 293 K in 1,1,2,2-tetrachloroethane-d_2.

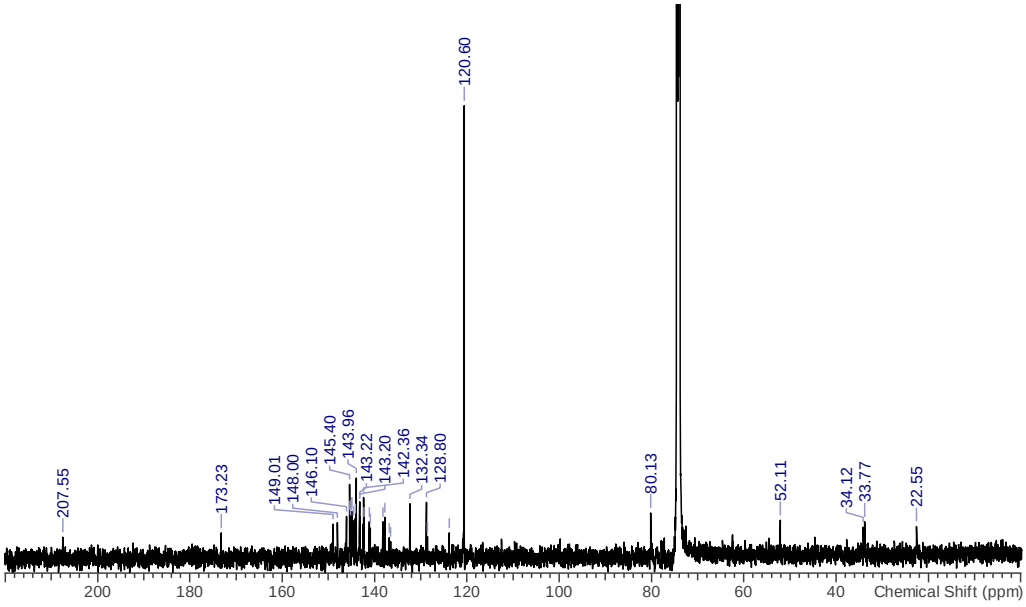


Figure S4. ^{13}C-NMR spectra of **(PCB)$_2$C$_2$** recorded at 293 K in 1,1,2,2-tetrachloroethane-d_2.

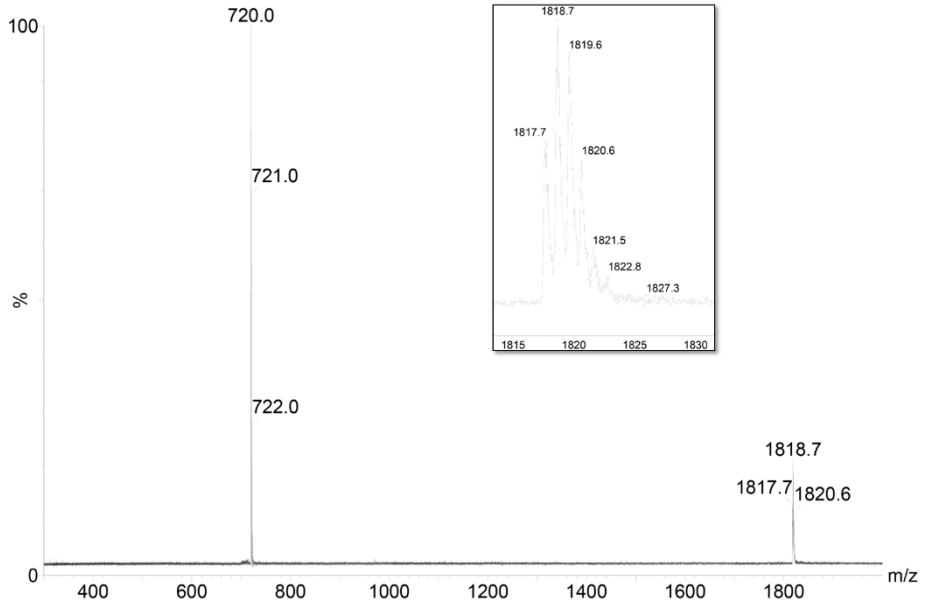


Figure S5. Negative ion MALDI mass spectrum of **(PCB)$_2$C$_2$**, using C_{60} (m/z: 720.0) as internal calibrant. The inset shows a zoomed view of the molecular ion peak.

[6,6]-Phenyl-C61-butyric acid 2-hydroxytetradeuteroethyl ester (*d*-PCBC$_2$OH). [6,6]-Phenyl-C61-butyric acid (**PCBA**) (400 mg, 0.45 mmol) was added to 80 mL of anhydrous *o*-

dichlorobenzene and sonicated during 20 minutes. After sonication the brownish suspension was heated to 110°C for two hours in order to fully dissolve the PCBA. The resulting black solution was cooled to 0°C in an ice-bath before ethylene glycol-d_4 (1 mL, 7.85 mmol) and 4-Dimethylaminopyridine (5.5 mg, 0.05 mmol) were added. Finally *N*,*N*'-Dicyclohexylcarbodiimide (101 mg, 0.49 mmol) was added to the reaction mixture, which was allowed to warm to room temperature and stirred overnight. The solvent was removed from the reaction mixture by rotary evaporation. The recovered crude product was purified by column chromatography on silica gel using a mixture of toluene:pyridine (95:5) as mobile phase. The recovered fractions were concentrated and precipitated into cold methanol. The title compound was recovered as a brown solid after filtration (107 mg, 0.11 mmol, 25 %). ^{1}H NMR (400 MHz, 1,1,2,2-tetrachloroethane-d_2) δ ppm 7.97 - 7.88 (m, 2 H), 7.60 - 7.42 (m, 3 H), 2.96 - 2.80 (m, 2 H), 2.55 (t, *J*=7.6 Hz, 2 H), 2.21 - 2.06 (m, 2 H). MS (MALDI-ToF): *m/z* calcd for $C_{73}H_{12}D_4O_3$ ($M^{\cdot-}$) 944.1, 945.1, 946.1, 947.1 found 944.1, 945.1, 946.1, 947.1.

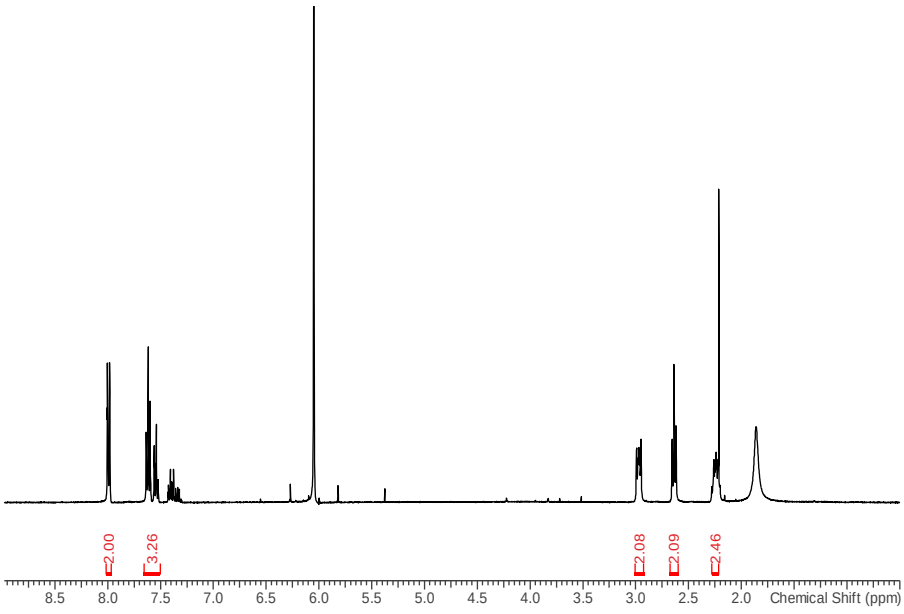


Figure S6. ^{1}H-NMR spectra of ***d*-PCBC$_2$OH** recorded at 293 K in 1,1,2,2-tetrachloroethane-d_2.

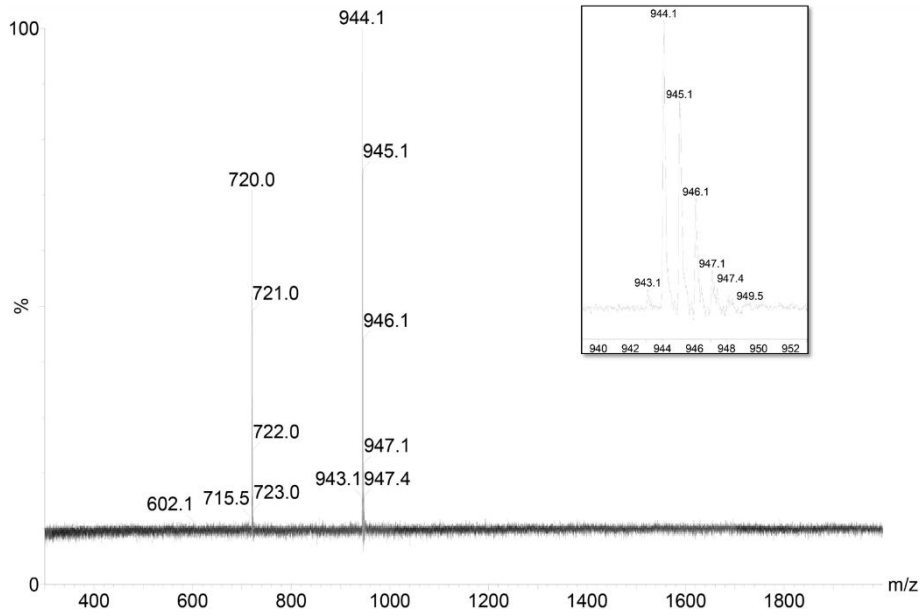


Figure S7. Negative ion MALDI mass spectrum of ***d*-PCBC$_2$OH**, using C_{60} (m/z: 720.0) as internal calibrant. The inset shows a zoomed view of the molecular ion peak.

Bis-[6,6]-phenyl-C61-butyric acid tetradeuteroethane-1,2-diyl ester (*d*-(PCB)$_2$C$_2$).

d-PCBC$_2$OH (95 mg, 0.10 mmol) was dissolved in 50 mL of anhydrous *o*-dichlorobenze and cooled to 0°C. PCBA (180 mg, 0.20 mmol) and 4-Dimethylaminopyridine (2.5 mg, 0.02 mmol) were added, before *N*,*N'*-Dicyclohexylcarbodiimide (45 mg, 0.22 mmol) was added. The reaction mixture was allowed to warm to room temperature and stirred overnight. Afterwards the solvent was removed from the reaction mixture and the recovered crude product was purified by column chromatography on silica gel using toluene as eluent. The recovered fractions were concentrated and precipitated into methanol. The title compound was recovered as a dark brown solid after filtration (26 mg, 0.01 mmol, 14%). ^{1}H NMR (400 MHz, 1,1,2,2-tetrachloroethane-d_2) δ ppm 7.99 - 7.96 (m, 2 H), 7.63 - 7.50 (m, 3 H), 2.97 - 2.92 (m, 2 H), 2.60 (t, *J*=7.4 Hz, 2 H), 2.24 - 2.19 (m, 2 H). MS (MALDI-ToF): *m/z* calcd for $C_{144}H_{22}D_4O_4$ ($M^{\cdot-}$) 1823.2, 1824.2, 1822.2, 1825.2 found 1822.7, 1823.7, 1821.7, 1824.6.

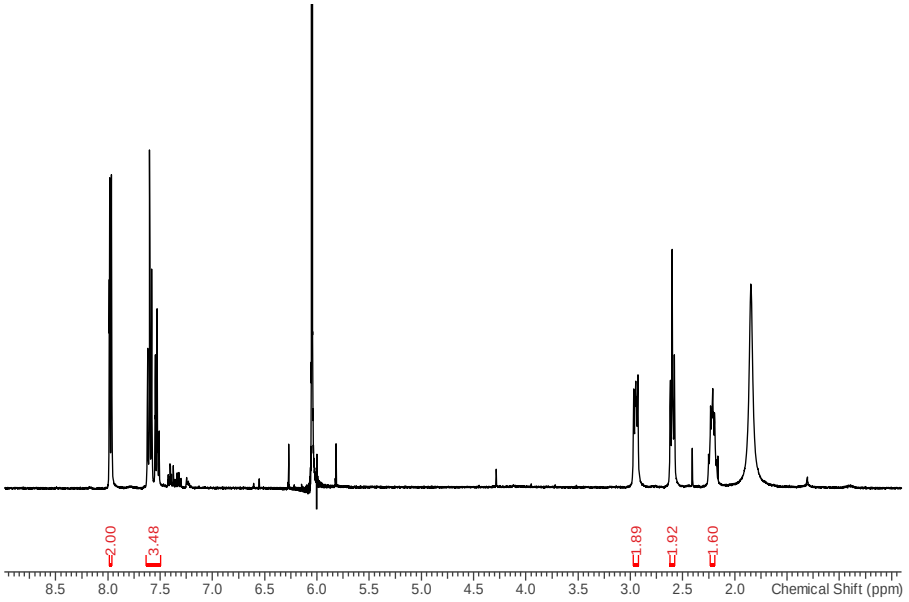


Figure S8. ^{1}H-NMR spectra of ***d*-(PCB)$_2$C$_2$** recorded at 293 K in 1,1,2,2-tetrachloroethane-d_2.

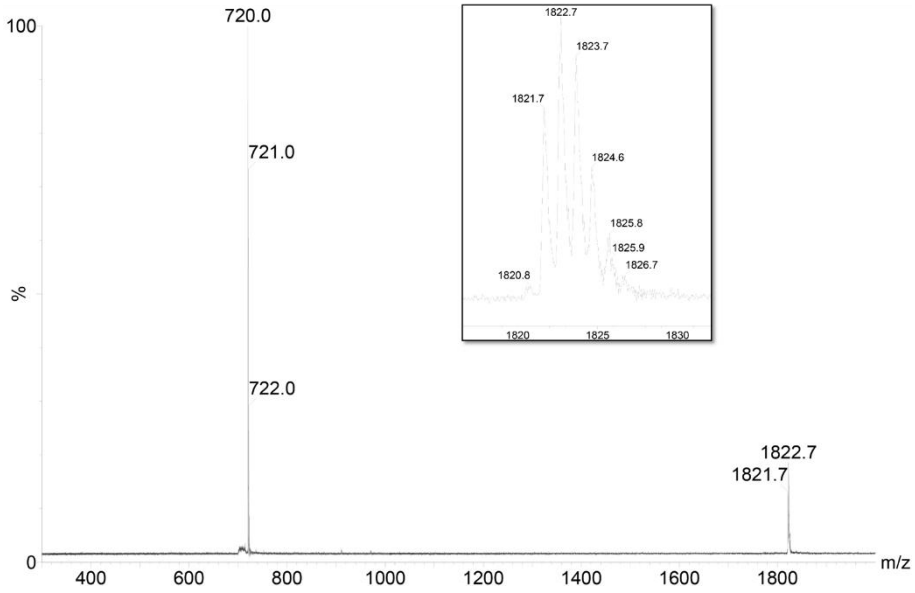


Figure S9. Negative ion MALDI mass spectrum of ***d*-(PCB)$_2$C$_2$**, using C_{60} (m/z: 720.0) as internal calibrant. The inset shows a zoomed view of the molecular ion peak.

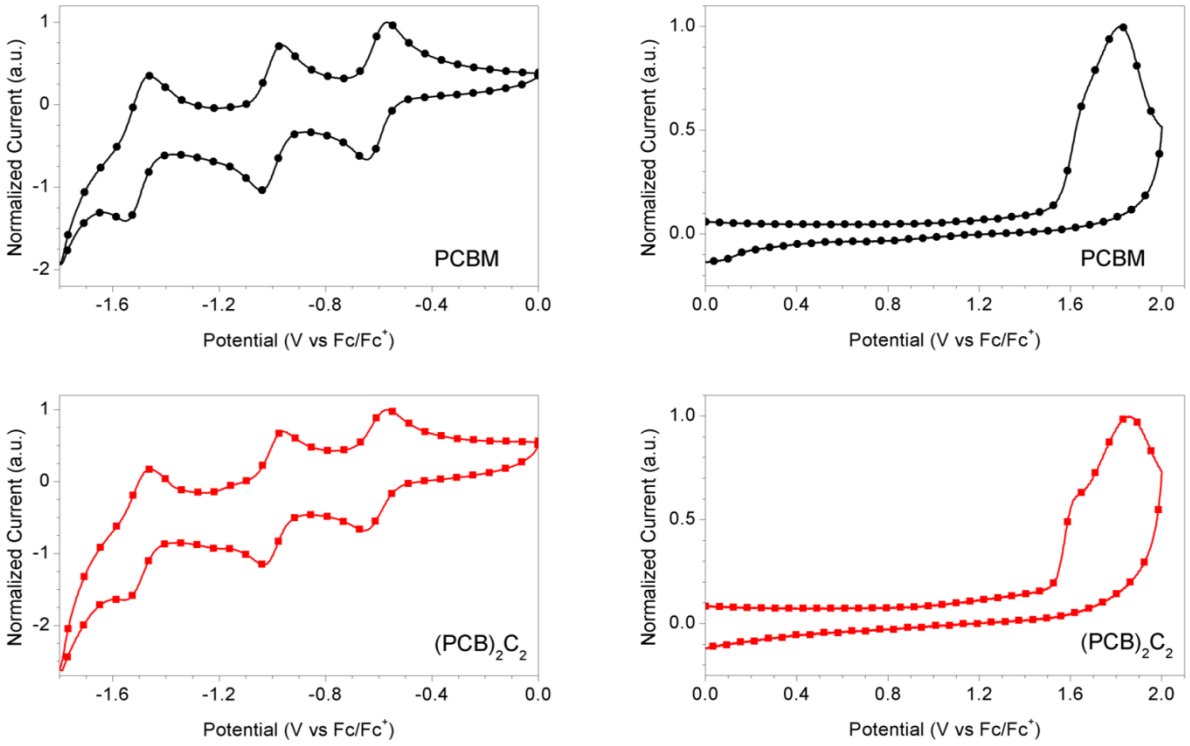


Figure S10. Cyclic voltammograms **PCBM** (top), respectively **$(PCB)_2C_2$** (bottom) were recorded at a scan rate of 100 mV/s in anhydrous *o*-dichlorobenzene solution with 0.1 M tetrabutylammonium hexafluorophosphate as the supporting electrolyte. Reductions are shown on the left and the oxidation cycles on the right.

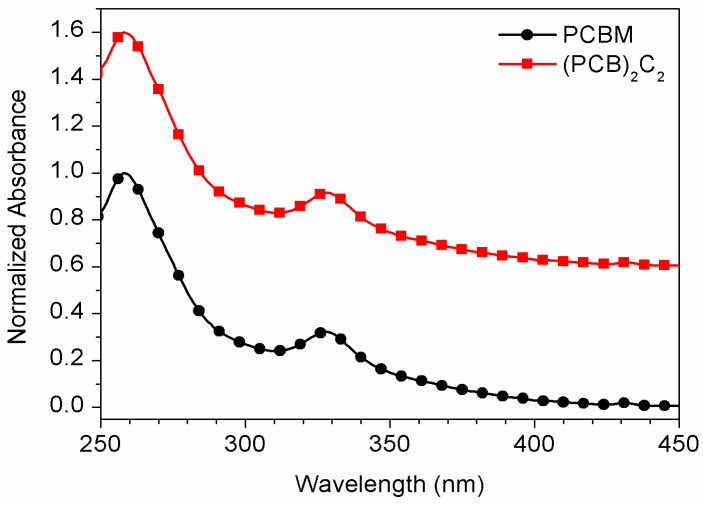


Figure S11. UV-*vis.* absorption spectra of **PCBM** and **$(PCB)_2C_2$** were recorded in dilute THF solutions at 25°C.

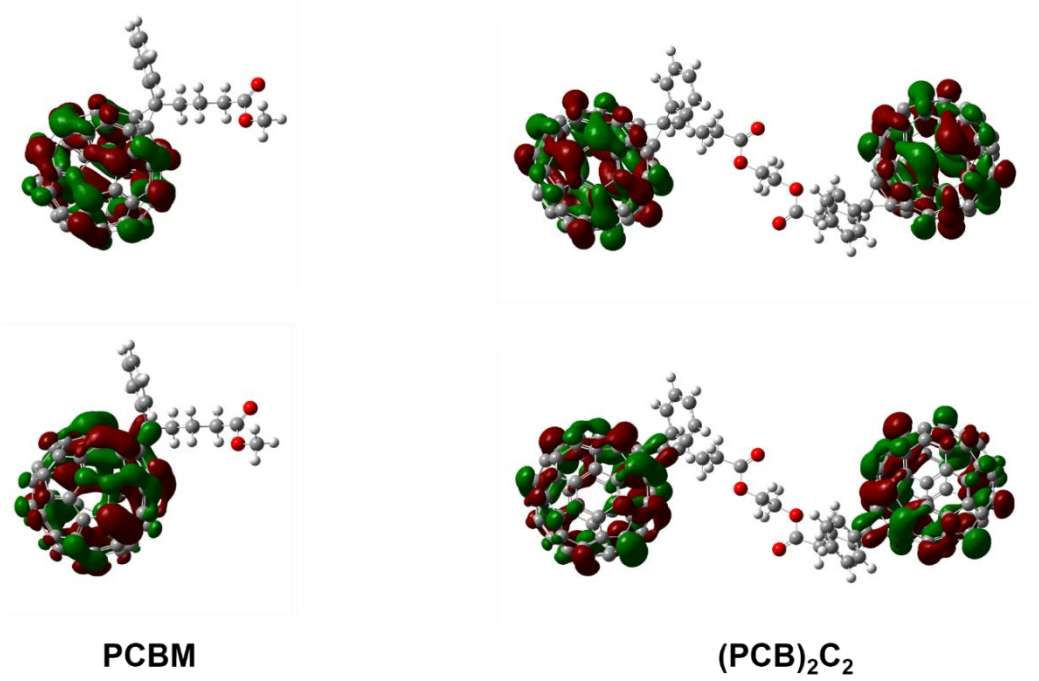


Figure S12. Energy-minimized structure (B3LYP/6-31G*) of **PCBM** and **$(PCB)_2C_2$** with visualization of the HOMO (bottom row) and LUMO (top row) wave functions. In case of **$(PCB)_2C_2$**, both HOMO and LUMO were found to be degenerate and the above wave function distributions represent the sum of both degenerate states for the HOMO and LUMO.

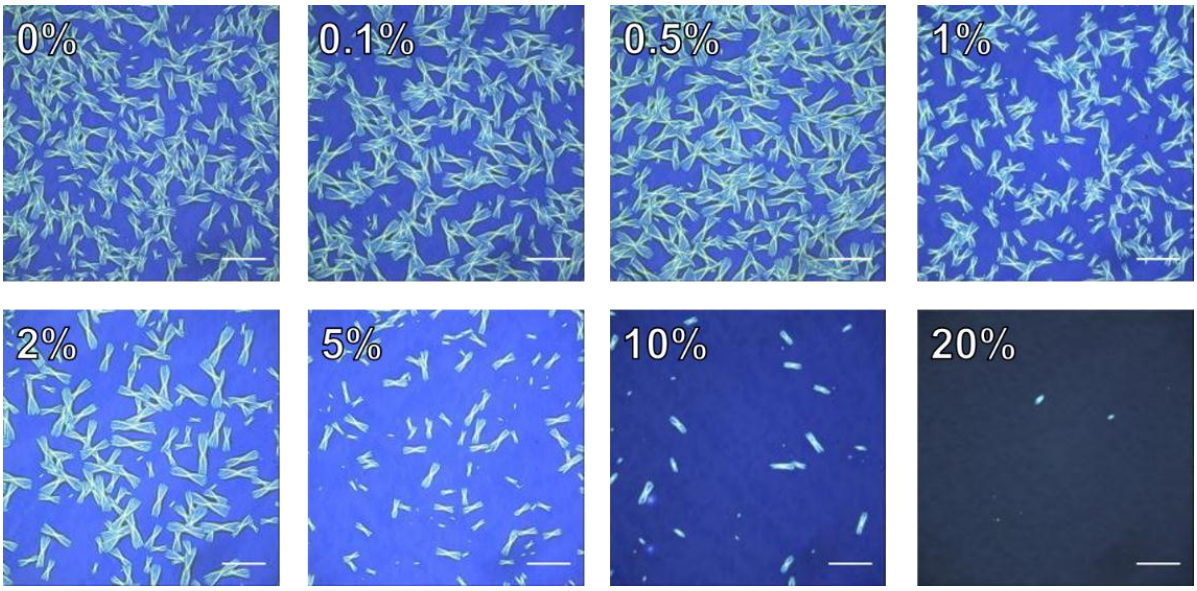


Figure S13. Optical microscope images of **PCDTBT**:fullerene (w/w 1:2) blends on silicon substrate with an increasing percentage of **$(PCB)_2C_2$**. All blend films were annealed under identical condition for 1 hour at 140°C prior to the measurement. Scale bar is 25 μm.

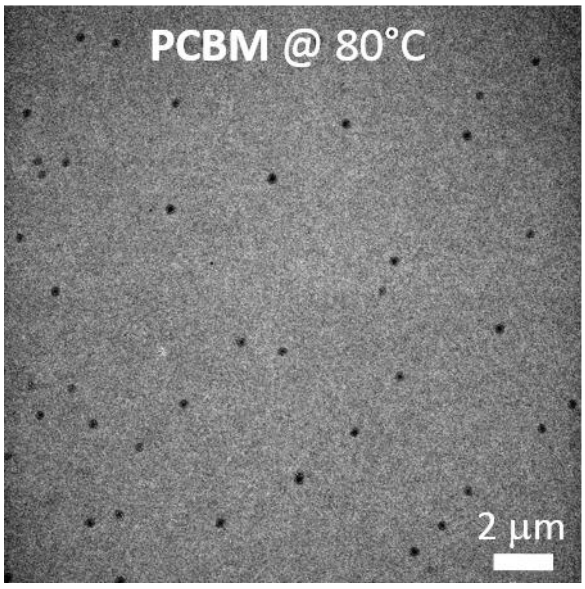


Figure S14. TEM micrographs of **PCDTBT:PCBM** films annealed 80°C prior to the measurement. Scale bar is 2 μm. **PCDTBT:PCBM** devices and **PCDTBT:PCBM:$(PCB)_2C_2$** (20%).

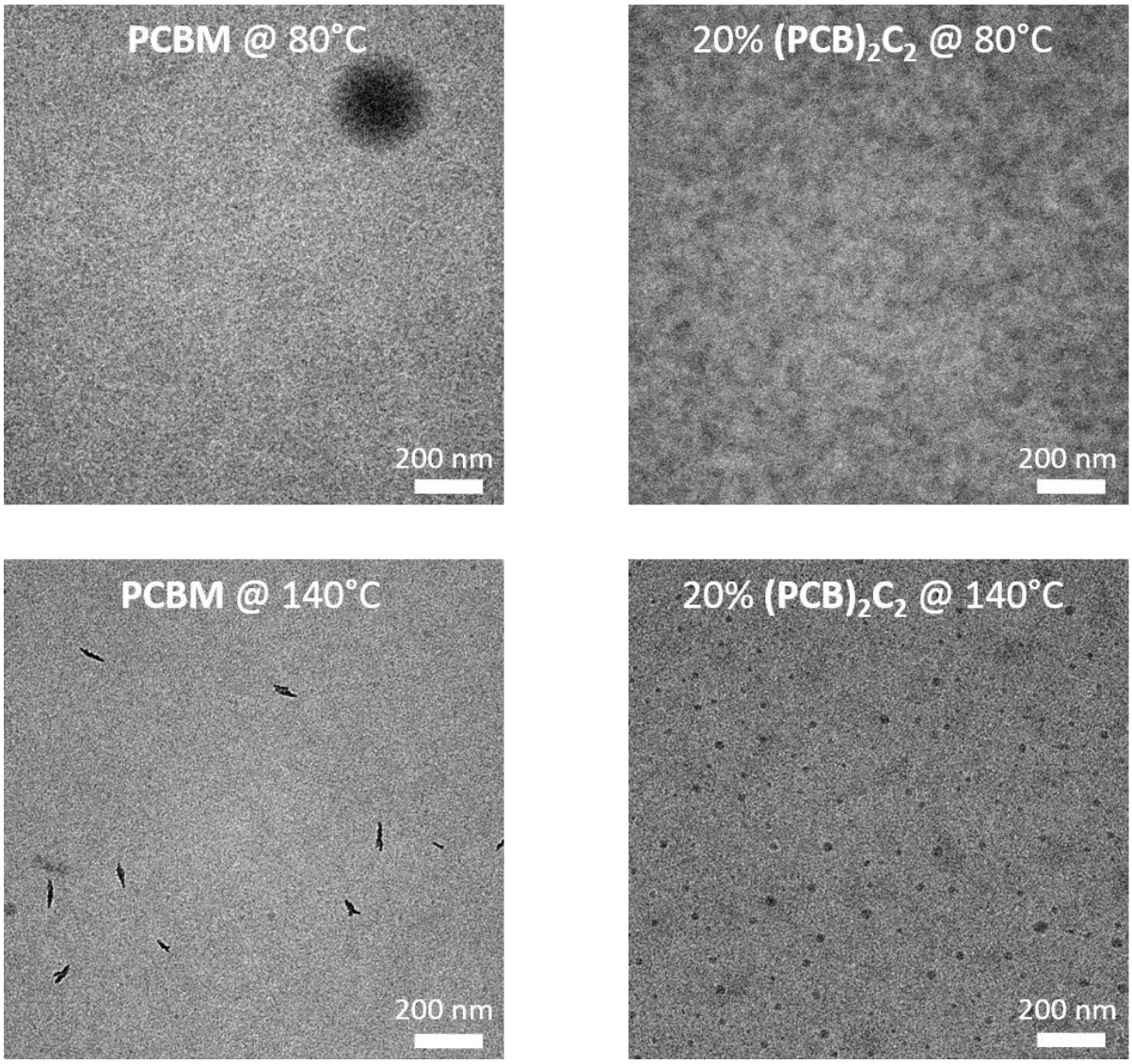


Figure S15. TEM micrographs of **PCDTBT:PCBM** film (left column) and **PCDTBT:PCBM:$(PCB)_2C_2$** (20%) (right column) annealed at the indicated temperatures prior to the measurements. Scale bar is 200 nm.

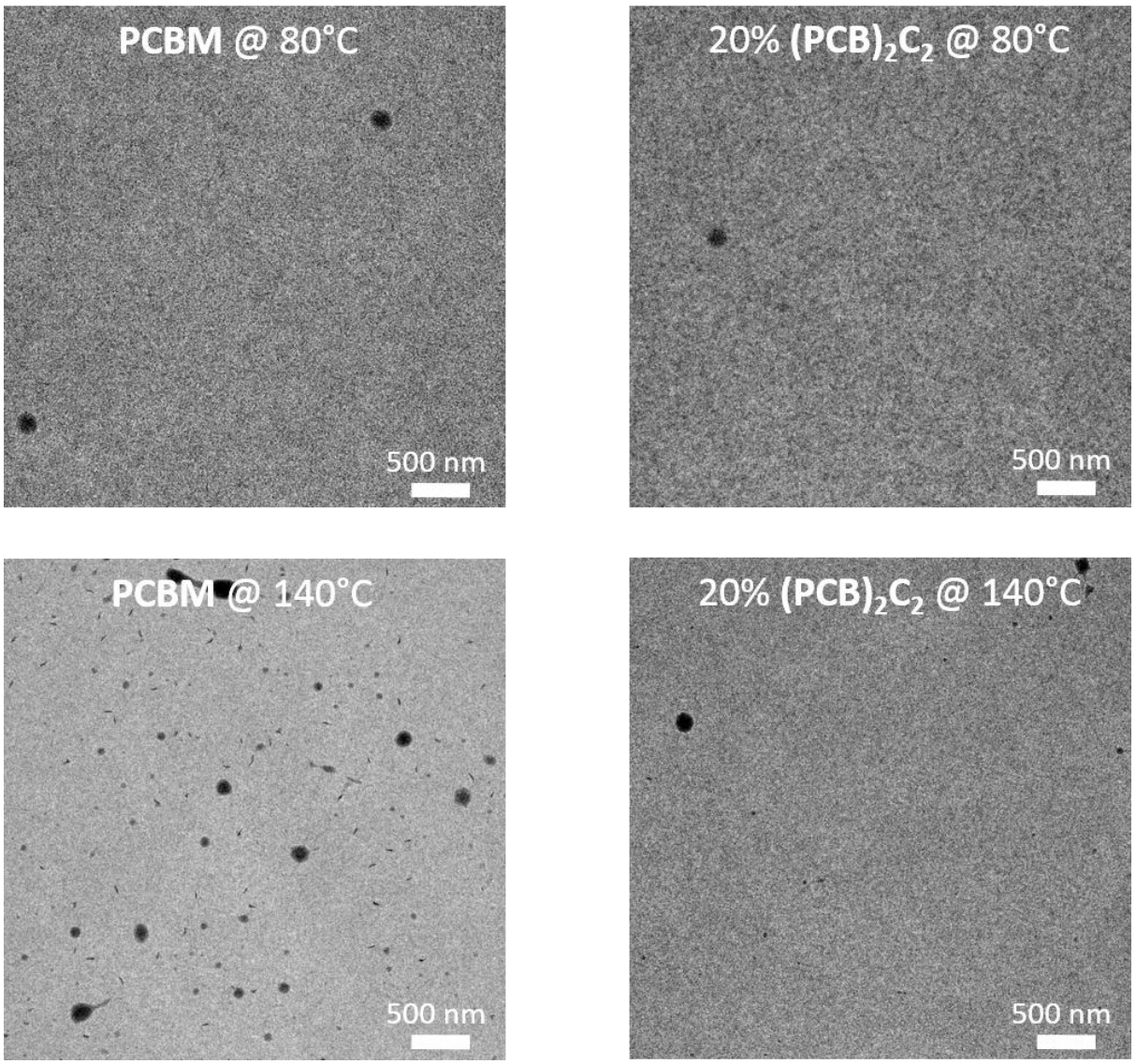


Figure S16. TEM micrographs of **PCDTBT:PCBM** film (left column) and **PCDTBT:PCBM:$(PCB)_2C_2$** (20%) (right column) annealed at the indicated temperatures prior to the measurements. Scale bar is 500 nm.

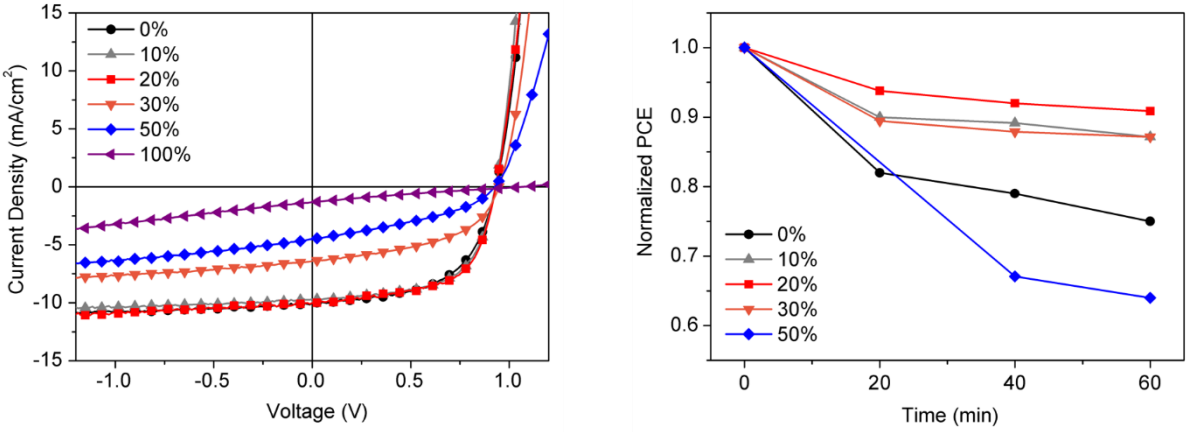


Figure S17. (Left) Comparison of the initial J-V characteristics of optimized conventional **PCDTBT:PCBM** devices containing different weight percentages of **$(PCB)_2C_2$** prior to thermal stability test. (Right) Degradation of solar cell PCE as a function of time at 85°C thermal stress in nitrogen atmosphere of optimized conventional **PCDTBT:PCBM** devices containing different weight percentages of **$(PCB)_2C_2$**.

Table S1. Initial device parameters of conventional **PCDTBT:PCBM** devices containing different loadings of the **$(PCB)_2C_2$**.

System	J_{sc} [mA/cm^2]	V_{oc} [V]	FF	PCE [%]
PCDTBT:PCBM	10.06	0.93	0.57	5.33
PCDTBT:PCBM:$(PCB)_2C_2$ (10%)	9.70	0.93	0.61	5.50
PCDTBT:PCBM:$(PCB)_2C_2$ (20%)	10.01	0.93	0.61	5.68
PCDTBT:PCBM:$(PCB)_2C_2$ (30%)	6.40	0.95	0.50	3.04
PCDTBT:PCBM:$(PCB)_2C_2$ (50%)	4.54	0.93	0.38	1.6
PCDTBT:$(PCB)_2C_2$ (100%)	1.34	1.07	0.21	0.3

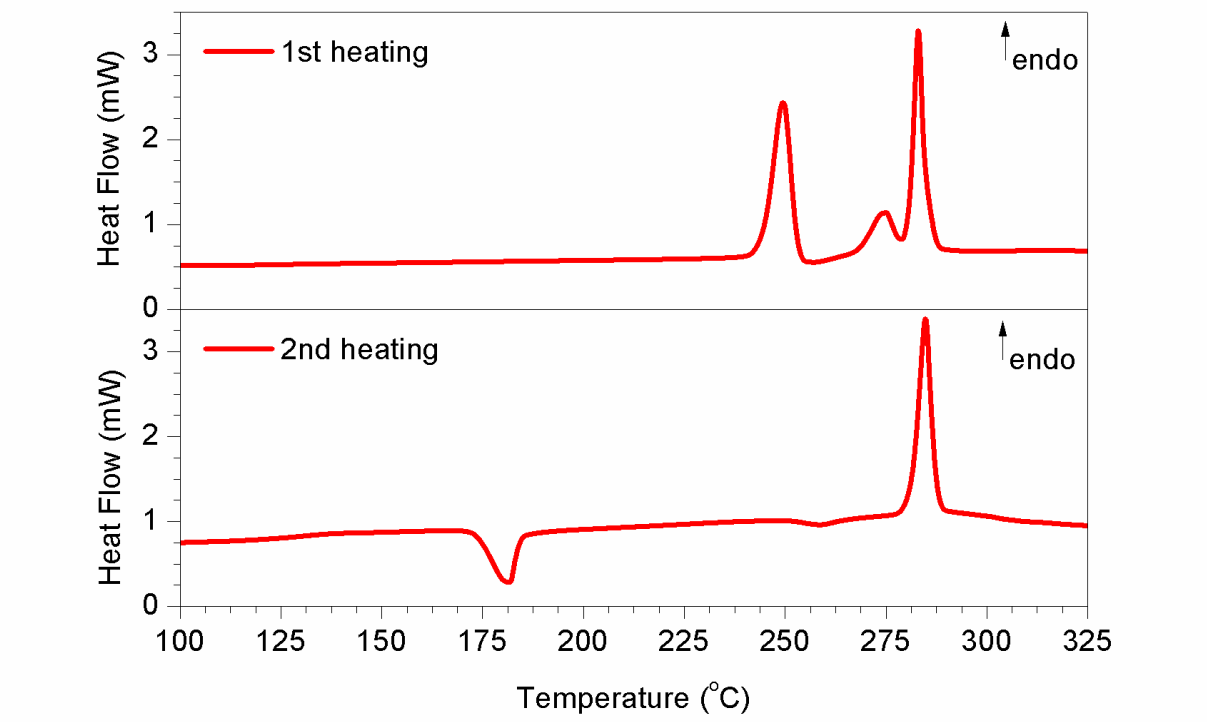


Figure S18. DSC traces of **PCBM** recorded at heating rate of 10°C/min..

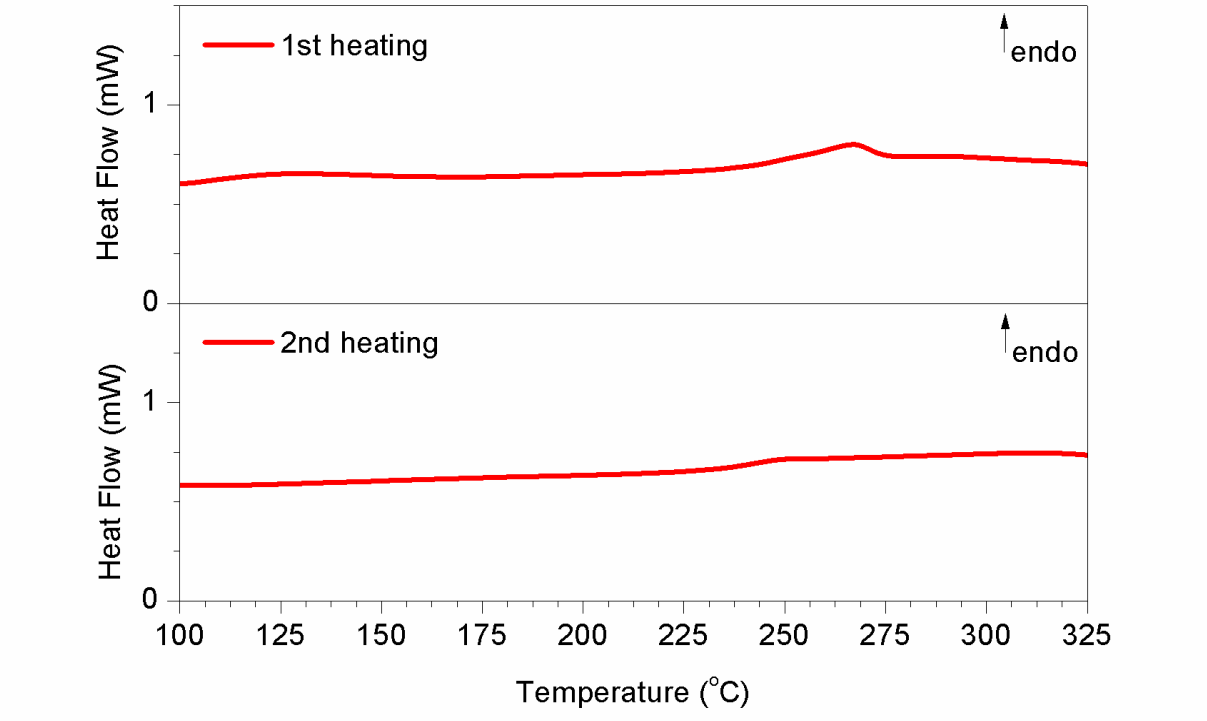


Figure S19. DSC traces of **$(PCB)_2C_2$** recorded at heating rate of 10°C/min..

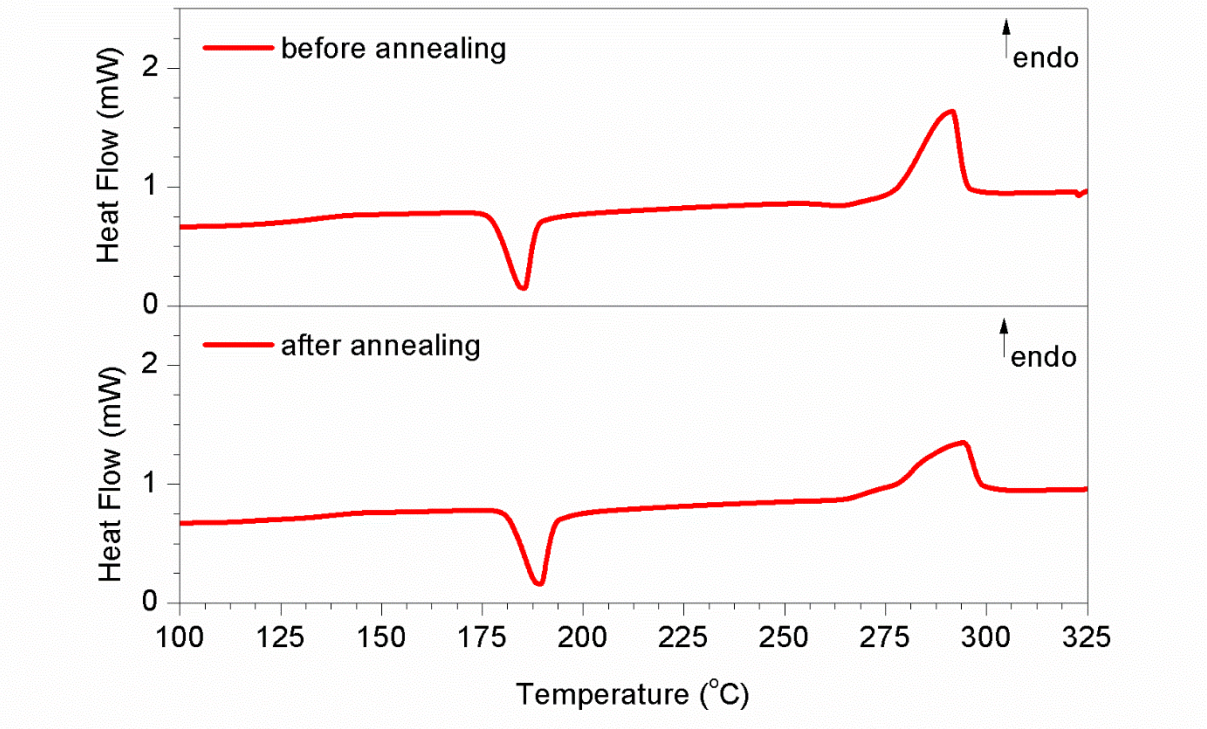


Figure S20. DSC traces of **PCBM** before 2 hour annealing at 85°C and after annealing, recorded at heating rate of 10°C/min..

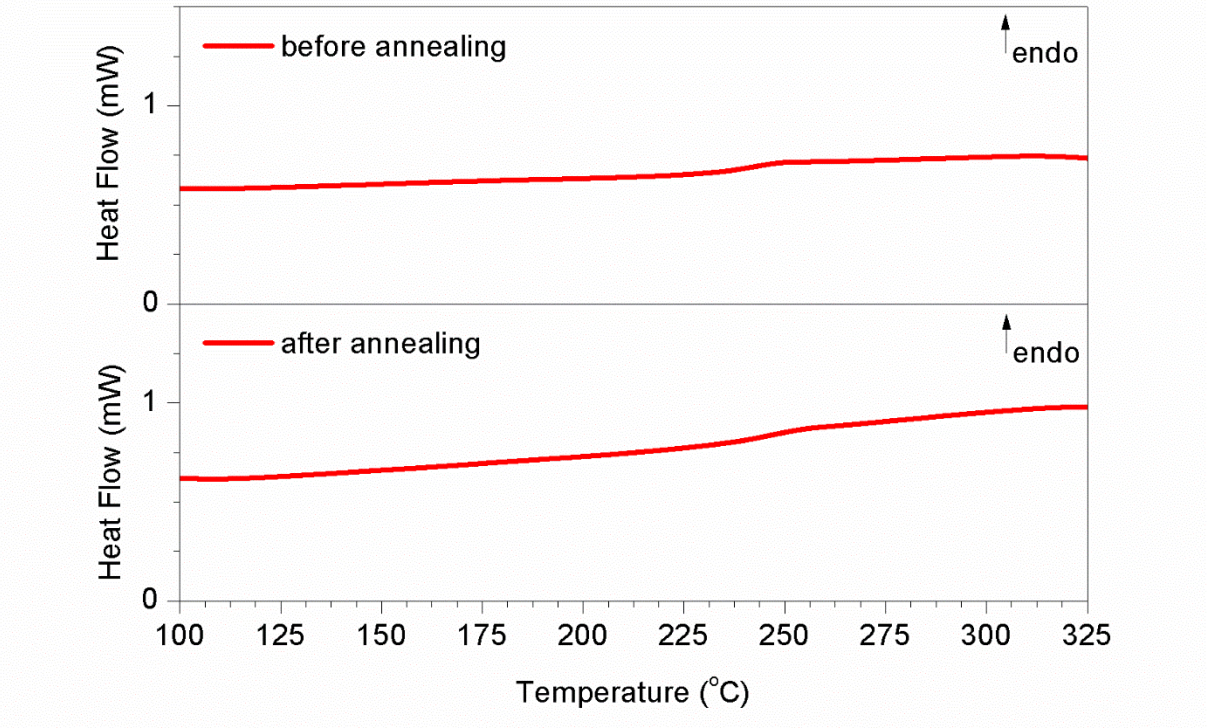


Figure S21. DSC traces of **$(PCB)_2C_2$** before 2 hour annealing at 85°C and after annealing, recorded at heating rate of 10°C/min..

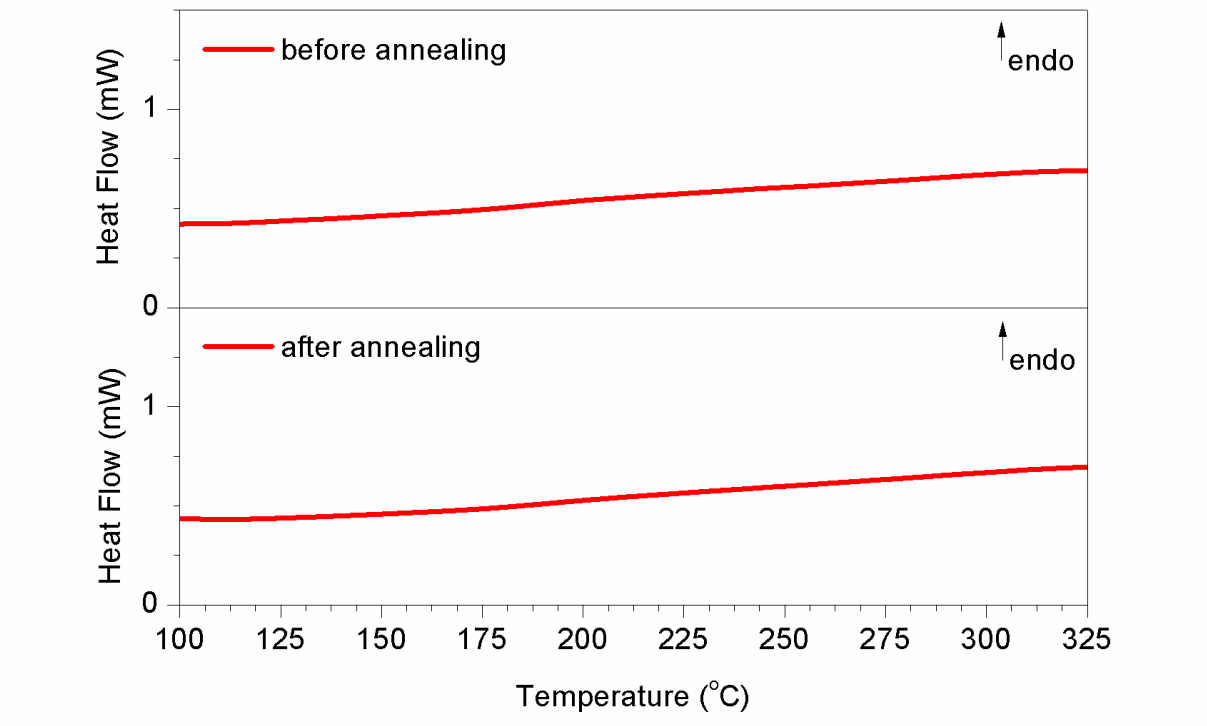


Figure S22. DSC traces of **PCBM:(PCB)$_2$C$_2$** (20%) before 2 hour annealing at 85°C and after annealing, recorded at heating rate of 10°C/min..

OFET